The lacustrine-water vapor isotope inventory experiment L-WAIVE

Patrick Chazette[1], Cyrille Flamant[2], Harald Sodemann[3], Julien Totems[1], Anne Monod[4], Elsa Dieudonné[5], Alexandre Baron[1], Andrew Seidl[3], Hans Christian Steen-Larsen[3], Pascal Doira[1], Amandine Durand[4], and Sylvain Ravier[4]

[1]Université Paris-Saclay, Laboratoire des Sciences du Climat et de l'Environnement (LSCE), CEA-CNRS-UVSQ, UMR CNRS 8212, CEA Saclay, 91191 Gif-sur-Yvette, France
[2]LATMOS/IPSL, Sorbonne Université, UVSQ, CNRS UMR 8190, Paris, France
Correspondence to: Patrick Chazette (patrick.chazette@lsce.ipsl.fr)
[3]University of Bergen, Bergen and Bjerknes Centre for Climate Research, Bergen, Norway
[4] Aix Marseille Univ, CNRS, LCE, Marseille, France
[5]Université du Littoral Côte d'Opale, Laboratoire de Physico-Chimie de l'Atmosphère (ULCO/LPCA), France

Correspondence to: Patrick Chazette (patrick.chazette@lsce.ipsl.fr)

Abstract. In order to gain understanding on the vertical structure of atmospheric water vapor above mountain lakes and to assess its link with small-scale factors, such as winds in a valley and synoptic scale subsidence in complex terrain, among others, the L-WAIVE (Lacustrine-Water vApor Isotope inVentory Experiment) field campaign was conducted in the Annecy valley in the French Alps in June 2019. This field campaign was based on a synergy between a suite of ground-based, boat-borne, and two ultra-light aircraft (ULA) measuring platforms implemented to characterise the thermodynamic and isotopic state above the lake environment using both in-situ and remote sensing instruments. A Cavity Ring-down Spectrometer and an in-cloud liquid water collector, were deployed onboard one of the ULA to characterize the vertical distribution of the main stable water vapor isotopes ($H_2^{16}O$, $H_2^{18}O$ and $H^2H^{16}O$) together with the temporal evolution of the tropospheric structure, thermodynamics and dynamics using a Mie-Rayleigh lidar, a Raman lidar and a wind lidar, respectively. ULA flight patterns were repeated several times per day to capture the diurnal evolution as well as variability associated with different weather events. Throughout the campaign, boat-borne lake temperature profiles as well as liquid water samples at the air-water interface and at 2 m depth in the lake thermocline were made, supplemented on one occasion by atmospheric water vapor isotope measurements from the boat. The campaign period included a variety of weather events leading to contrasting humidity and cloud conditions, slope wind regimes and aerosol contents in the valley. A significant variability of the isotopic composition was observed along the time within the first 1.5 km above ground level (a layer defined as the lake region of influence, below the average height of the mountains surrounding the lake) depending on weather conditions, as well as local and synoptic atmospheric circulations. We also highlight that fairly well-mixed conditions prevailed in the lower free troposphere in this first 1.5 km above the lake. Moreover, it is shown that strong gradients of isotopic composition can be observed at higher altitudes depending on the mean mountains height, the vertical local stability and the synoptic circulation.

Keywords: L-WAIVE, valley, lake, Annecy, stable water isotopes, aerosol, lidar, airborne

1   Introduction

The regions surrounding mountain lakes are poorly documented, yet they are highly anthropized, as in the case of Alpine lakes, which are suffering from significant ecological upheavals probably linked to climate change, which influences the rates of precipitation and ice melt. Water resources and biodiversity are under threat. Lake/atmosphere interactions significantly regulate the climatic conditions in the valleys. There is therefore an obvious societal importance in studying the undeniable role of this ecosystem on the water cycle, which makes a major contribution to maintaining biodiversity in these regions.

Why is the vertical structure of the water vapor field in the lower troposphere only sparsely documented above Alpine lakes? This is in part due to the complexity and fast-evolving nature of the low-level atmospheric circulation in Alpine-type valleys which is intimately linked to the orography surrounding the lakes interacting with the synoptic scale circulation. Thermally driven wind systems may be induced by hilly terrain, such as slope, mountain, and plateau winds (Kottmeier et al., 2008). Such winds result in mountain venting phenomena that control the variability of the water vapor field in mountain catchment on very small-time scales. Furthermore, small-scale inhomogeneity in soil properties across a mountain valley, as well as lake breezes resulting from land-lake temperature contrasts, may also induce the development of thermal circulations, particularly on clear-sky days, modifying the wind, humidity, and temperature fields on small spatial scales. The interaction of slope-driven and secondary circulations can furthermore influence the thermodynamical environment in the valley by the formation of convergence lines. Such convergence lines may favour the formation of shallow clouds, and in some cases even deep convection (Barthlott et al., 2006). Interaction with the synoptic scale circulation can lead to the formation of strong, gusty down-valley winds such as foehn events (Drobinski et al., 2007) and gap flows (Flamant et al., 2002; Mayr et al., 2007) that can also contribute to rapid modifications of the water vapor field in mountain catchment areas.

Stable water isotopes have long been used as a tool to study processes in lacustrine and hydrologic systems (see review by Gat, 2010), as well as evapotranspiration (e.g. Berkelhammer et al., 2016). For instance, an early study based on water stable isotope measurements conducted in the US Great Lakes region suggested that in the summer up to 15% of the atmospheric water content in the atmosphere downwind of the lakes is derived from lake evaporation (Gat et al., 1994). Isotopic measurements of lake water have shown the relative roles of evaporation from the lake surface and transpiration from surrounding vegetation (Jasechko et al., 2013). The link between hydrology and evaporation has mainly been investigated using vapor and liquid water isotopes measurements gathered just above the Earth's surface and samples from lake water and precipitation (e.g. Cui et al., 2016).

Unexploited potential remains to use stable water isotopes for increasing our understanding of the influence of evaporation, boundary-layer processes, and the free troposphere for local and regional climate conditions in Alpine lakes. For example, the depth of the atmospheric layer over which the influence of evaporation from the lake surface is detectable, and how different factors control the depth of this layer are still largely unknown. Detailed and comprehensive analysis of small-scale factors,

such as winds in a valley, and how they are related to the mesoscale and large-scale dynamics, such as synoptic scale subsidence in complex terrain, are therefore needed.

In order to get insights into such aspects, the L-WAIVE (Lacustrine-Water vApor Isotope inVentory Experiment) field campaign was conducted in the Annecy valley (45°47' N, 6°12' E, in Haute-Savoie in the French Alps) around the Annecy lake between 12 and 23 June 2019. Being the second largest natural, glacial lake in France, the Annecy lake is expected to play a substantial role for the regional hydrometeorology. The overarching scientific objective of L-WAIVE field campaign is to study evaporation processes and their heterogeneity over the Annecy lake using an original multi-platform instrumental approach based on continuous high-resolution vertical profiling of tropospheric water vapor, temperature and wind as well as aerosols in the valley, together with airborne and boat-borne measurements of stable water isotopes ($H_2^{16}O$, H^2HO and $H_2^{18}O$) in vapor, as well as liquid water sampling in the lake, in clouds, and from precipitation.

We have defined such an observation strategy including ultra-light aircraft (ULA) means because measurements from tall towers only provide incomplete information on the link between evaporation and atmospheric processes in the free troposphere, such as mixing and distillation (e.g. Griffis et al., 2016; Steen-Larsen et al., 2013). In the past, He and Smith (1999) combined airborne measurements and surface sampling of the water isotope composition to study the evaporation process over the forests of New England, however before the advent of high-resolution laser-based spectrometers. More recent available airborne measurements of the isotope composition in the boundary layer either focused on areas above sea (Sodemann et al., 2017), or did not include measurements of the surface isotope composition (Salmon et al., 2019). The use of ULAs makes it possible to sample the atmosphere very close to the surface up to altitudes of more than 4000 m and to fly in deep valleys (Chazette et al., 2005).

The main objective of this paper is to present a novel experimental approach to measure stable isotopes of water from the interior of steep valleys to the free troposphere in order to help identifying the origin of the air masses that contribute to the observed isotope ratios. This paper provides an overview of L-WAIVE campaign observational strategy and its most innovative aspects (use of multiple ULAs, ULA-borne CRDS measurements, isotopologues sampling in the vapor and liquid phase in the environment of the Annecy lake, …) as well as the description of involved instrumental assets. The paper also presents first scientific highlights from the L-WAIVE experiment and proposes a consolidated vision of water isotopologues across the air/water compartments in a lake area. The experimental strategy is discussed in Section 2 whereas the instrumental platforms operations, environmental variables monitoring are presented in section 3. In Section 4 we give the synoptic condition of atmospheric circulation that help to understand the temporal evolution of the measurements in the valley, and more generally the meteorological conditions encountered during the field campaign. Atmospheric water vapor and liquid water isotopes, as well as lake water isotope observations made across the valley are described in Section 5. In Section 6, we summarize and conclude.

2   L-WAIVE experimental strategy

To achieve the scientific and methodological objectives of the L-WAIVE project, the field campaign was implemented in the southern part of the Annecy lake (the so called "Petit Lac"), in the vicinity of the city of Lathuile (Fig. 1). The Annecy lake is bordered by the city of Annecy to the north, the Massif des Bauges to the west (2217 m above mean sea level – a.m.s.l.), the Massif des Bornes to the East (2438 m a.m.s.l.) and the depression de Faverges to the south (where Lathuile is located). Lathuile is located east of the foothill of the Roc des Boeufs (1774 m a.m.s.l.) to the west of the "Petit Lac" and the Tournette summit (2350 m a.m.s.l.) to the east. The Annecy lake, at a mean altitude of 446.7 m a.m.s.l., covers an area of roughly 27.5 km^2, and has a mean (maximum) depth of 41.5 m (82 m).

Figure 1. Geographical location of L-WAIVE. The different pictures give a view of the environment where the measurements were performed and of the instrumented platforms used: a) location of the experiment, b) lake water sampling from a boat, c) instrumented van, d) instrumented ultra-light aircrafts, and e) panoramic view from UAV showing the location of Lathuile, as well as the Roc des Boeufs to the left, the Tournette summit to the right and the "Petit Lac" in between.

2.1   Measurement platforms

Three airborne, one boat-borne and one ground-based instrumented platforms were deployed in the vicinity of Lathuile in order to monitor humidity, temperature, wind, clouds and aerosols in the lower troposphere over the Annecy lake and the

surrounding valley environment, as well as to conduct measurements at the interface between the atmosphere and the lake, and in the lake. A brief overview of the platforms is given below, whereas the details on the instrumental payloads are given in Section 3:

    i)   Airborne platforms:

        a.   One ultra-light aircraft (ULA) was mainly dedicated to remote sensing measurements. It allowed exploring the two or three-dimensional structure of the lower troposphere thanks to a polarized Rayleigh-Mie lidar. It also carried a meteorological probe (pressure, temperature, relative humidity), an aerosol particle sizer and two visible flux meters for the upward and downward solar radiations to complement the lidar measurements and determine the surface albedo in the visible spectrum. This will be referred to as "aerosol ULA" (ULA-A) in the following.

        b.   A second ULA carried both a Cavity Ring-down Spectrometer (CRDS) water vapor isotope analyser, a meteorological probe for pressure, air temperature, Global Positioning System (GPS) location and relative humidity, and a cloud water collector. The platform offers the opportunity to measure the vertical profiles of temperature, relative humidity, H^2HO, $H_2^{18}O$ and $H_2^{16}O$ and to collect cloud water samples. The latter were collected during specific cloud flights (when meteorological conditions were favourable) and the cloud collector was opened only in clouds. We will refer to this platform as "isotope and cloud ULA" (ULA-IC) in the following.

        c.   An Unmanned Aerial Vehicle (UAV) acquired vertical profiles of temperature, relative humidity, and pressure in the surface layer (first 150 m above the ground level) using a meteorological probe.

    ii)   Ground-based platform: Simultaneous high-resolution vertical profiles of water vapor, temperature, aerosols and winds were acquired continuously from two co-located ground-based lidars.

    iii)   Boat-borne platform: An instrumented boat allowed sampling the lake water by vials at the surface film and underneath (~2 m deep) for the assessment of H^2HO and $H_2^{18}O$. A probe was also used to assess the vertical profiles of water temperature below the surface down to a depth of 55 m. A CRDS water vapor isotope analyser performed measurements during one day at the end of the experiment just above the lake surface in parallel with the lake water sampling.

These different platforms are presented in Fig. 1 together with a view of the experiment site.

2.2   Deployment

Depending on the weather conditions, airborne platforms were deployed several times a day to document the temporal evolution of the atmospheric boundary layer over the lake. The days of operation of all platforms are summarized in Table A1

of Appendix A. The ground-based water vapor, temperature and aerosol lidar operated continuously between 12 and 21 June in the morning (gathering over 220 h of data), while the ground-based wind lidar (WL) operated continuously between 14 and 23 June in the morning (acquiring also over 220 h of data). The UAV performed 7 flights between 13 and 21 June. A total of 22 successful flights were conducted with ULA-A between 13 and 19 June, while ULA-IC performed 15 flights between 14 and 20 June. The 15 ULA-IC flights were tightly coordinated with ULA-A flights. Valid cloud water samples were only obtained during the last 3 ULA-IC flights. The CRDS previously installed on ULA-IC was mounted on the boat from 21 to 22 June. Boat-borne CRDS observations were made at the surface of the lake on the last outings of the boat. Up to 12 lake water temperature profiles were made between 13 and 21 June (sometimes twice a day) while lake water samples were made on 14 occasions. Finally, 28 samples of precipitation were made during the campaign (7 of which on 15 June in the afternoon) between 11 and 22 June 2019. The distribution of the precipitation samples with time as seen in Table A1 gives an indication as to when rain was encountered during the campaign, i.e. essentially at the beginning (14 and 15 June) and at the end (21 and 22 June) of the field deployment. In the meantime, clouds were regularly observed above the lake as documented by the ground-based lidars.

It is worth noting that all platforms (2 ground-based lidars, 2 ULA, 1 UAV, 1 boat) performed coordinated operations on 16, 17, 18, 19 and 20 June. These are considered as "golden days" and will be analysed in priority. A few less optimal days ("silver days") have also been defined based on the fact that 5 out of 6 instruments were simultaneously in operations, namely: 13 and 21 June. 21 June stands out as being a day when both precipitation water samples, and boat borne CRDS were acquired and will also be an analysis priority.

On days when both ULA flew coordinated patterns (13, 16-20 June), flights typically began with a profiling sequence between the surface and ~4 km a.m.s.l. which was carried out in the vicinity of the 2 ground-based vertically pointing lidars (see Fig. 2). Soundings with levelled legs (see blue dotted line in Fig. 2a) were performed at a relatively slow ascent rate (~60 m min⁻¹) to ensure that the instruments were as close as possible to equilibrium with the environment. Upon reaching 4 km a.m.s.l., the flight route of the 2 ULA differed, ULA-A performing a high-altitude survey above the Annecy lake (see red dotted line in Fig. 2a), while ULA-IC was aiming for shallow cumulus clouds to sample cloud water droplets as illustrated in Fig. 2b showing the instrumental synergy that took place during L-WAIVE. Liquid water sampling was performed via multiple passes through the clouds to accumulate enough material to conduct isotope analysis. At the end of the flight, both ULA performed race-track descents around the ground-based lidars on their way back to the airfield.

During ascent and descent, the airborne lidar ALiAS onboard ULA-A was pointing sideways to directly derive the aerosol extinction coefficient (Chazette et al., 2007; Chazette and Totems, 2017). For the exploration of the valley at a cruising altitude between 3.5 and 4.5 km a.m.s.l., ALiAS was pointing to the nadir. The combination of both flight sequences thus allowed to survey the 3-dimensional structure of the lower troposphere over the lake and its surroundings. The individual flight characteristics (time, maximum altitude, type of exploration) are presented in Appendix B for the two ULAs (Tables B1 and B2 for ULA-A and ULA-IC, respectively).
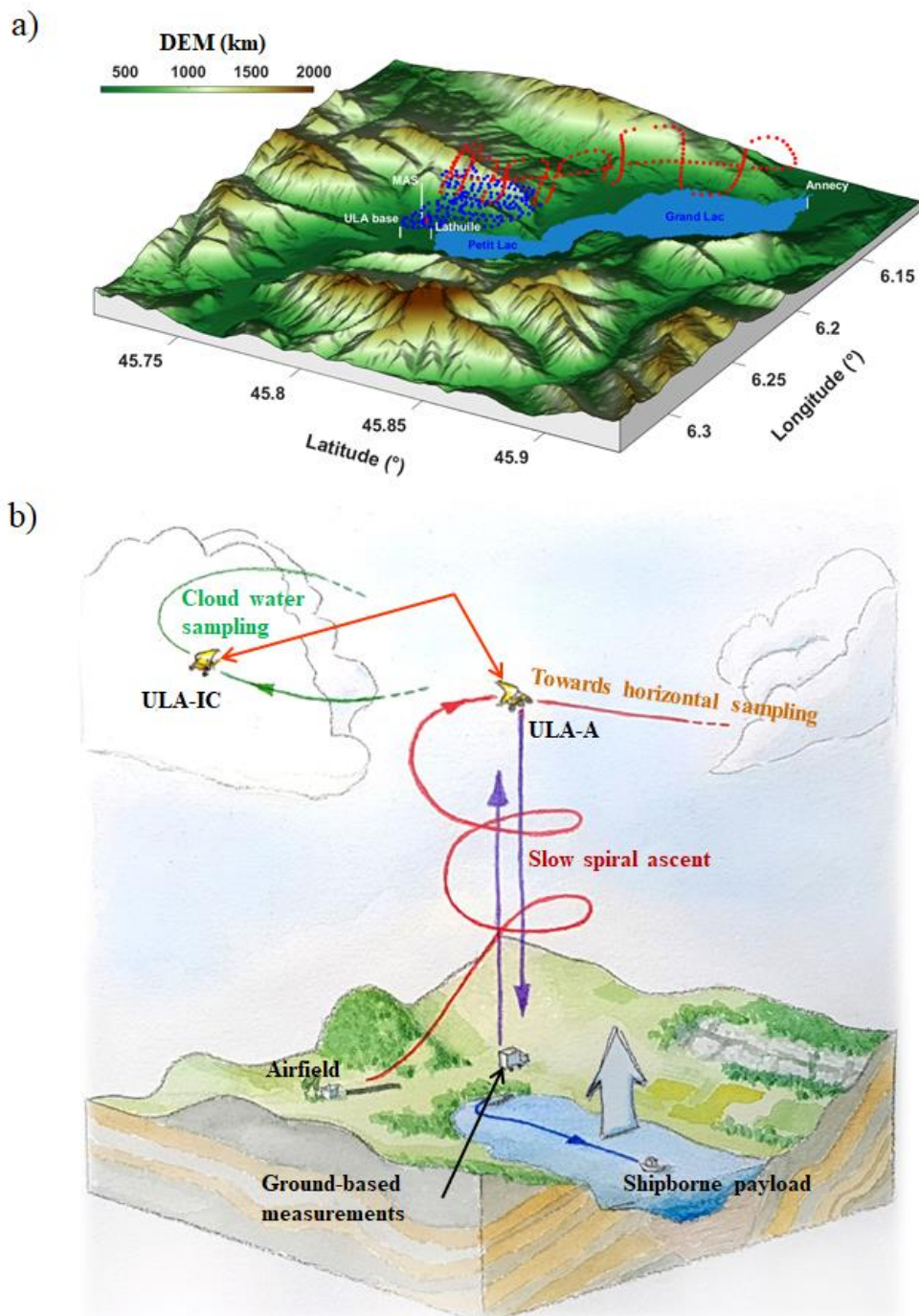
Figure 2. Example of a typical ULA flight plan performed during L-WAIVE (performed on 17 June 2019. a) The flight track adopted during the flight (blue dots for vertical profiling and red dots for horizontal exploration above the lake). DEM is for digital elevation model. b) Schematic representation of the measurement strategy adopted during L-WAIVE. Two types of sampling strategy are illustrated, red for atmospheric sampling and green for cloud sampling. The purple arrows illustrate that the atmospheric sampling is performed during both ascent and descent.

180

3 Instrumental set up on each platform

This section provides a detailed description of the payloads on all platforms deployed during L-WAIVE. The periods of operation of each measurement platform are given in Appendix A.

3.1 Airborne payloads

We used two Tanarg 912 XS ULA from the company Air Création (Chazette and Totems, 2017). For each ULA (ULA-A and ULA-IC, Fig. 3), the maximum total payload is of approximately 250 kg including the pilot. Flight durations were between ~1 and 2 hours, depending on flight conditions, with a cruise speed around 85-100 km h^{-1}. The ULA location was provided by a GPS and an Attitude and Heading Reference System, which are part of the MTi-G components sold by XSens.
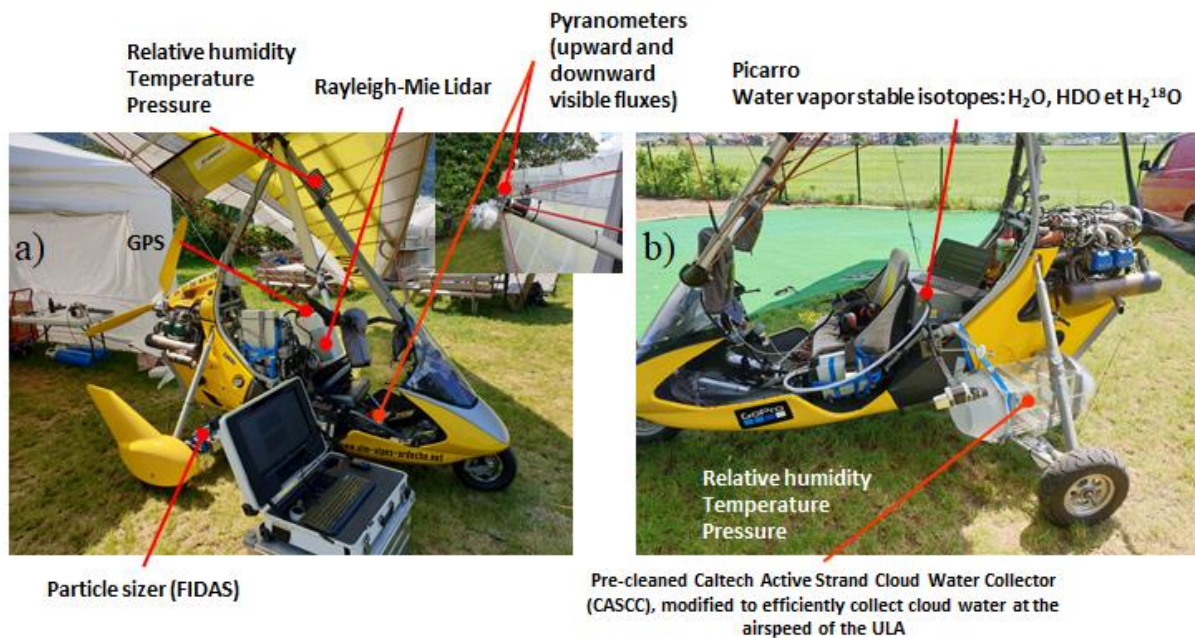
Figure 3. Ultra-light aircraft payloads: a) remote sensing payload with the Rayleigh-Mie lidar ALiAS (ULA-A) and b) in situ payloads with the CRDS isotope analyser and the Caltech Active Strand Cloud Water Collector (ULA-IC).

3.1.1 ULA-A

Rayleigh-Mie lidar. The Airborne Lidar for Atmospheric Studies (ALiAS) was especially developed by LSCE as an airborne payload dedicated to aerosols and clouds samplings (Chazette et al., 2012, 2020). It emits a pulse energy of 30 mJ in the ultraviolet at 355 nm with a 20 Hz pulsed Nd:YAG laser (ULTRA) manufactured by QUANTEL™ (https://www.quantel-laser.com/). The acquisition system is based on a PXI (PCI eXtensions for Instrumentation) technology. The receiver contains two channels for the detection of the elastic backscatter from the atmosphere in the parallel and perpendicular polarization planes relative to the linear polarization of the emitted radiation. The native resolution along the line-of-sight is 0.75 m, it is

degraded to 15 m during the data treatment to improve the signal to noise ratio. The wide field-of-view of ~2.3 mrad ensures a full-overlap of the transmit and receive paths close to 200-300 m from the emitter.

Visible flux-meters. Two pyranometers Kipp and Zonen™ CMP22 are mounted on ULA-A to determine the short-wave surface albedo. One is placed at the top of the wing's central mast to measure the downward flux and the other is placed under the cradle to measure the upward flux. The CMP22 pyranometer measures solar irradiance over the wavelengths from 200 to 3600 nm, with a directional error lower than 5 W m^{-2}.

Meteorological probe. Part of ULA-A payload was a shielded meteorological probe VAISALA PTU-300 for measuring temperature, pressure and relative humidity. This probe measures the atmospheric pressure, with a 1-minute sampling time, within an uncertainty of 0.25 hPa, the air temperature within an uncertainty of 0.2 K and relative humidity (RH) within a relative uncertainty of 2.5%.

Particle sizer. The granulometer used on board ULA-A was a FIDAS mobile manufactured by PALAS (https://www.palas.de/en/). The particle sizer operates on battery power with a volume flow of 1.4 l min^{-1} in environmental conditions of temperature, atmospheric pressure, and relative humidity (no drying). The particle size distribution is determined from 180 nm to 20 µm by means of an optical aerosol spectrometer using Lorenz-Mie scattered light analysis. The LED source homogeneously illuminates an optically differentiated measurement volume with white light. Each particle moving through this volume generates a scattered light impulse detected at an angle of 85° to 95° degrees. The amplitude of the impulse is a measure of the particle diameter and the particle number corresponds the number of impulses. To allow in-flight measurement while limiting the loss of particles, a sampling head has been designed and printed in 3D in order to guarantee an isokinetic air flow at the entrance of the FIDAS.

3.1.2 ULA-IC

CRDS water vapor isotope analyser. ULA-IC carried a CRDS water vapor isotope analyser (L2130-i, Picarro Inc., Sunnyvale, USA; Ser. No. HIDS2254) for the in-situ measurement at about 5 Hz of the $H_2^{16}O$ mixing ratio, and the isotope ratios $\delta^{18}O$ and δ^2H for $H_2^{18}O$ and H^2HO, respectively. Water vapor was drawn into the spectrometer through an unheated inlet of 68 cm length (1/4 inch O.D. stainless steel with Silconert coating), pointing backward on the left side of the aircraft at a distance of 38 cm from the CRDS. Pointing forward next to the vapor inlet, a fast-response temperature and humidity probe (iMet XQ-2, InterMet systems, USA; Ser. No. 61124) measured thermodynamic properties (T, RH, p with uncertainties of 0.3 K, 5 %, and 1.5 hPa, respectively) and GPS location at 1 Hz. The CRDS analyser was operated in flight mode, with a flow of about 150 sccm through the inlet maintained by a membrane pump (Part No. S2003, Picarro Inc.). Pressure and water vapor mixing ratio were corrected using calibration functions established at the FARLAB laboratory, University of Bergen, Norway. Raw measurements of the isotope parameters, expressed as δ-values (see Appendix C) were corrected for the mixing ratio-isotope composition dependency and calibrated across the campaign period following recommendations from the International Atomic Energy Agency (IAEA, see Appendix D for details). Tests with a small bubbler system during the campaign indicated

an anomaly in the CRDS measurements during 18-20 June, partially affecting two flights in the morning of 19 June, and the first flight on 20 June. The anomaly was due to a saturated inlet system from condensate forming on the aircraft during a cloud sampling flight on 18 June. Flight periods affected by inlet saturation effects were excluded from further analysis (see Appendix D).

In the afternoon of 19 June 2019, the two ULA performed a coordinated ascent, providing an intercomparison of response times and measurement offsets regarding pressure, temperature, and relative humidity on the two aircraft (Fig. 4). During the entire ascent sequence, there is a small, visually discernible temperature offset between the two instrumental packages (Fig. 4b). This offset originates from the slower response time of ULA-A instrumental package (red line), lagging behind ULA-IC the faster and more exposed iMet probe (black line). The relative humidity measurement on ULA-IC is clearly faster, and resolves structures in more detail (Fig. 4c, black line). A comparison of the specific humidity calculated from iMet and the laser spectrometer revealed similar response times (not shown). The intercomparison between the two ULAs and the two humidity measurements onboard ULA-IC thus also provides a first-order in-flight validation of the water vapor measurements of the CRDS analyser.

A time resolution better than 0.1 Hz was obtained for specific humidity from the CRDS and iMet probe, providing a spatial resolution of 200-300 m in horizontal direction, and 10-50 m in the vertical, assuming a typical horizontal speed of 85-100 m s^{-1} and ascent rate of the aircraft of about 1-5 m s^{-1}. Due to more complex memory effects, the isotope composition has lower effective time resolution (Sodemann et al., 2017; Steen-Larsen et al., 2014). We use here 10 s average data for all parameters on ULA-IC from upward profiles, filtered for rapid elevation changes, defined as exceeding 1.0 hPa ascend or 1.0 hPa descend within 10 s.
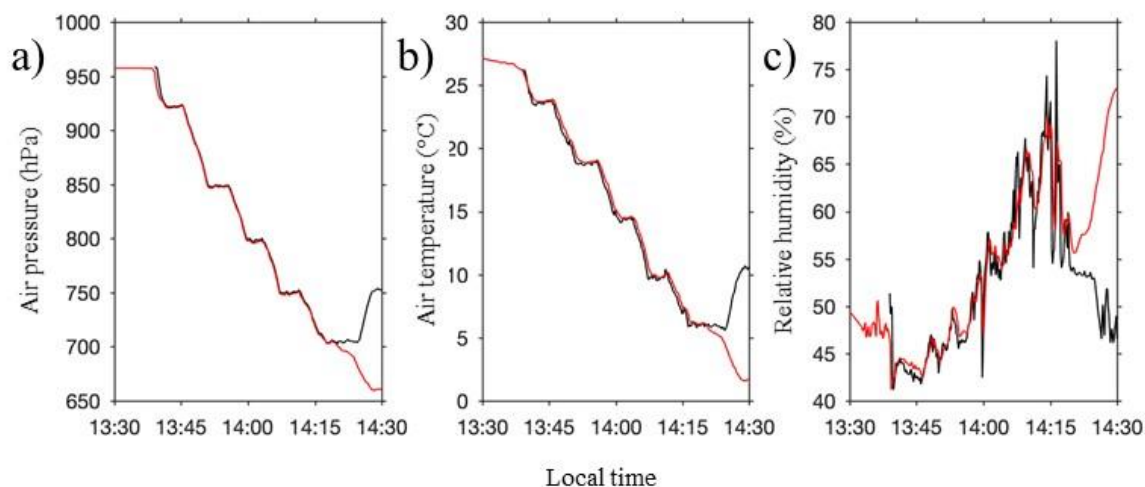
Figure 4. Comparison between (a) air pressure (hPa), (b) air temperature (°C) and (c) relative humidity (%) between the meteorological probes mounted on ULA-A (red line) and ULA-IC (black line) during coordinated flights in the afternoon of 19 June 2019.

Cloud water collector. A pre-cleaned Caltech Active Strand Cloud Water Collector (CASCC, Demoz et al., 1996) was mounted on ULA-IC, modified to efficiently collect cloud water (Fig. 3b) at the relative cruising speed of the ULA (85 to 100 km h^{-1}). The CASCC was modified to efficiently collect cloud liquid droplets from the ULA. In order to sample droplets under the same conditions as those obtained on the ground, the CASCC fan was removed, and its inlet and outlet were prolonged with convergent and divergent High-Density PolyEthylene (HDPE) cones to ensure an isokinetic air sampling. All parts necessary to adapt the HDPE cones on the CASCC were made of plastic. The flow through the probe must be steady and as turbulence-free as possible. The design of these modified inlet and outlet was calculated to get a constant mass of water droplets per time unit through the probe onboard the ULA. The resulting probe was installed on the side of the ULA where the flow was assumed laminar and allowed air sampling with a flow rate of 35 to 47 m^3 min^{-1}, ahead of the motor exhaust (Fig. 3b). The CASCC strings and inlet were pre-cleaned with deionized water prior each flight and covered with a clean plastic bag when not in-cloud (especially during take-off and landing). For a flight of 10 minutes inside a shallow cumulus cloud, the probe typically collected 41 to 48 g of cloud liquid droplets corresponding to a liquid water content of 0.10 to 0.16 g m^{-3}, typical for such cloud type (Herrmann, 2003).

3.2   Ground-based instrumentation

The ground-based scientific facility hosted by the technical department of the city of Lathuile was mainly composed of the Raman lidar WALI and of a scanning Doppler lidar. WALI was embedded in the ground-based MAS (mobile atmospheric station; Raut and Chazette, 2009). The UAV was also operated from this site, close to the lidar. Figure 5 shows the two lidars and the UAV.
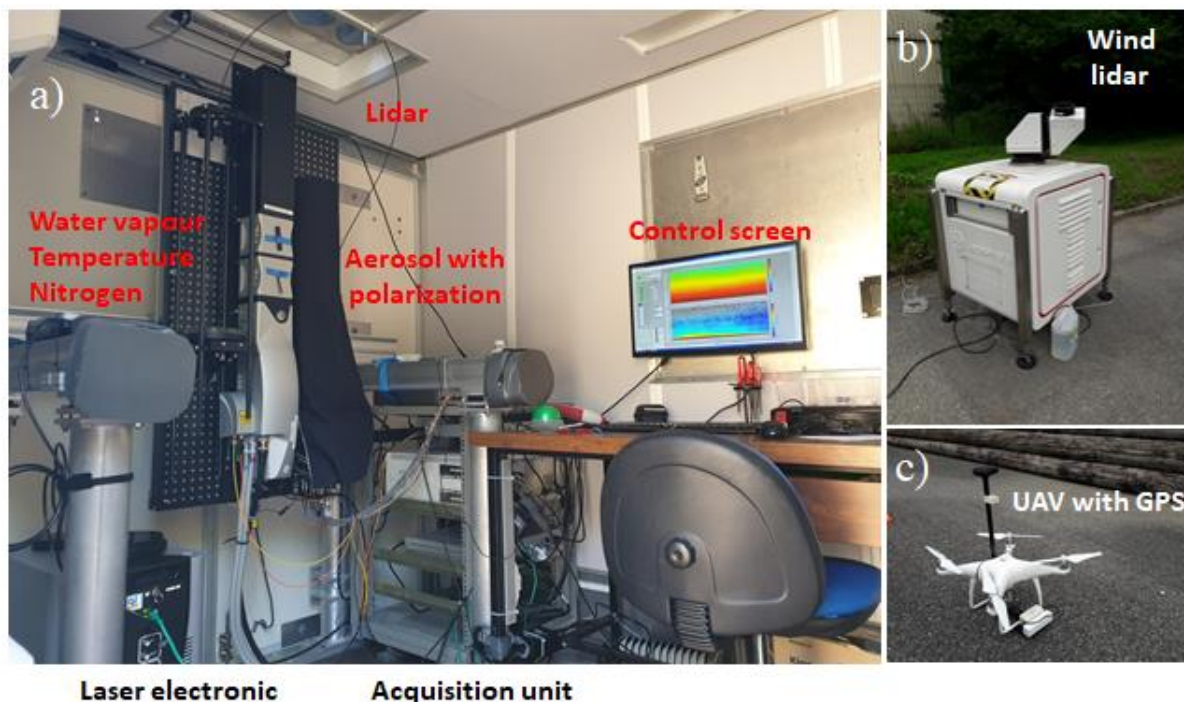
Figure 5. a) Lidar WALI on board the mobile atmospheric station (MAS), b) wind lidar located close to the MAS, and c) UAV with its GPS antenna (in black).

3.2.1 Raman lidar

WALI has been developed at LSCE (Chazette et al., 2014) based on the same technology as its precursor instruments LESAA (Lidar pour l'Etude et le Suivi de l'Aérosol Atmosphérique; Chazette et al., 2005) and LAUVA (Lidar Aérosol UltraViolet Aéroporté, Chazette et al., 2007; Lesouëf et al., 2013; Raut and Chazette, 2009). It is a custom-made instrument dedicated to atmospheric research activities.

The lidar operates with an emitted wavelength of 354.7 nm and is designed to fulfil eye-safety standards (EN 60825-1). Its emitter is a pulsed Nd:YAG laser (Q-smart 450 by Quantel™) with a fibre laser injector to stabilize the emitted wavelength. The acquisition system is based on a PXI (PCI eXtensions for Instrumentation) technology manufactured by the National Instruments™ company, and contains 12 bits digitizers at 200 MS/s corresponding to a native vertical resolution of 0.75 m. During the entire experiment, the acquisition was performed for mean profiles of 1000 laser shots leading to a native temporal sampling close to 1 minute. The UV pulse energy was ~70 mJ and the pulse repetition frequency was 20 Hz. The wide field-of-view of ~2.3 mrad allows a full-overlap of the transmission and reception paths beyond ~ 200-300 m. Note that the pulse energy decreased linearly with time due to a laser failure, from 70 mJ to about ~50 mJ at the end of the campaign.

The receiver is composed of 2 distinct detection paths, both using small collector diameters of 15 cm, with a low full-overlap distance (~150-200 m). The first path is dedicated to the detection of the elastic molecular, aerosols and cloud backscatter from

the atmosphere. Two different channels are implemented on that path to detect i) the total (co-polarized and cross polarized with respect to the laser emission) and ii) the cross-polarized backscatter coefficients of the atmosphere. The second path, a fibered achromatic reflector, is dedicated to the measurements of the atmospheric Raman scattering, namely the vibrational signal for nitrogen (N_2-channel) and water vapor (H_2O-channel) and the rotational signal to derive the temperature (T-Channel).

The water vapor mixing ratio (WVMR) is retrieved with an absolute error less than 0.4 g kg^{-1} in the first 2 km above the ground level (a.g.l.) (Chazette et al., 2014; Totems et al., 2019). The calibration of the T-channel is derived from the methodology presented by Behrendt (2006) and leads to an absolute error on the temperature lower than 1 °C within the first 2 km a.g.l. The final vertical resolution is set to 15 m below 1 km a.g.l. and 30 m above, and the temporal resolution is 0.5 h. In the following, a temporal resolution of 1 h is used.

3.2.2   Wind lidar

Wind profiles were measured using a scanning Doppler lidar (Leosphere Windcube WLS100). It operates in the infrared (1.543 µm) with a low pulse energy (0.25 mJ) but a high pulse repetition frequency (20 kHz). The Doppler shift due to the particles' motion along the beam direction (radial wind speed) is determined through heterodyne detection followed by fast Fourier transform analysis. The acquisition time was set to 1 s during the campaign. The pulse duration is 200 ns, corresponding to an axial resolution of 50 m given the pulse shape, with a minimal and maximal range of 100 m and 7.2 km, respectively. The axial resolution can be lowered to 25 m by reducing the pulse duration (100 ns) while increasing the pulse repetition frequency (40 kHz) which in turn reduces the minimal and maximal range to 50 m and 3.3 km, respectively. In practice, the maximum range is limited by the signal level. A minimum Carrier to Noise Ratio (i.e. signal to background noise ratio) of −27 dB is required to keep the radial wind uncertainty (determined from the spectrum peak width) below 0.5 ms^{-1}. Therefore, observations in the free troposphere are possible only when elevated layers of aerosols are present. Even in the boundary layer, several days of very low aerosol load occurred during the campaign, in which case the Carrier to Noise Ratio threshold was lowered to −30 dB. With such a low Carrier to Noise Ratio, the measurements must be considered with caution.

Profiles of the three components of the wind vector were determined using the Doppler Beam Swinging technique originally proposed for Doppler radar (e.g. Koscielny et al., 1984). Here, the measurement cycle includes one vertical beam, for which the radial wind is the vertical component of the wind vector, and four slanted beams (15° from zenith) in the cardinal directions to derive the two horizontal components of the wind. During L-WAIVE, the lidar alternated between 20 cycles of 25 m-resolution profiles and 20 cycles of 50 m-resolution profiles. The uncertainty on the horizontal / vertical wind components is determined using the variability inside averaging periods, possibly gathering several measurement cycles. Regarding the effects of orography, corrections to the wind profiles are needed when working over sloping terrain or on top an elevated area (Bradley et al., 2015). During the campaign, the Doppler lidar was positioned in a wide valley (~3 km at the observation site)

with a rather flat bottom, and the closest distance existing between one of the slanted beams and an obstacle was ~1 km. Therefore, the influence of the orography on the measurement are assumed to be negligible here.

3.3 Boatboard payload: Lake and atmospheric sampling

325 The lake water surface and subsurface were sampled at the middle of the "Petit Lac" to measure water isotopes and chemicals from the boat:

i) The lake water thermal stratification was monitored using an EXO sonde, equipped with temperature, pressure, pH, dissolved dioxygen, ion conductivity and chlorophyll sensors. Profiles recorded in the middle of the "Petit Lac" (Fig. 1) once or twice per day (Table A1) and showed that the thermocline (Fig. 6) was typically at a depth 330 of about 7 to 13 m, in good agreement with previous studies of the Lake (Danis et al., 2003).

ii) Subsurface water samples were collected at a depth of 2 m in HDPE capped flasks. Surface water samples were collected using a 30 x 30 cm silica glass plate immersed into water for a minute, then gently removed from water vertically (Cunliffe et al., 2013). The water falling from the plate in a continuous flow was not sampled, then, the dropwise water was collected in HDPE capped flaks. The surface microlayer samples were then collected by 335 scraping the remaining water on the glass plates (using a rubber scraper) in amber glassware capped vials. All liquid water samples were measured for isotopic composition ($H_2^{18}O$, $H^2H^{16}O$) at FARLAB, University of Bergen according to established laboratory procedures (Appendix D).

iii) On 22 June, the CRDS isotope analyser was taken on board the boat to sample a cross-section in the atmospheric layer just above the "Petit Lac" through the location used for in situ sampling on the other days. This made it 340 possible to capture the isotope concentrations as a function of the distance from the shore and the depth of the lake on that day. Water vapor isotope measurements were taken from an inlet at either ~20 cm or ~2 m above the water surface, while the iMet sonde measured temperature, relative humidity and location. Post-processing and calibration of water vapor measurements were done as for the aircraft data (Sec. 3.1.2).

3.4 Precipitation sampling

345 Precipitation samples were taken throughout the campaign period. The sampling device consisted in a pre-cleaned HDPE funnel directly connected to a pre-cleaned HDPE sampling bottle. The precipitation samples were manually operated: after each precipitation event, the sample was aliquoted into 1.5 ml glass vials with rubber/PTFE septa and stored at 4°C prior to isotopic analysis, while the rest of the sample was stored at -18°C. Precipitation sampling times lasted from 20 min to several hours, depending on rainfall rate.

350
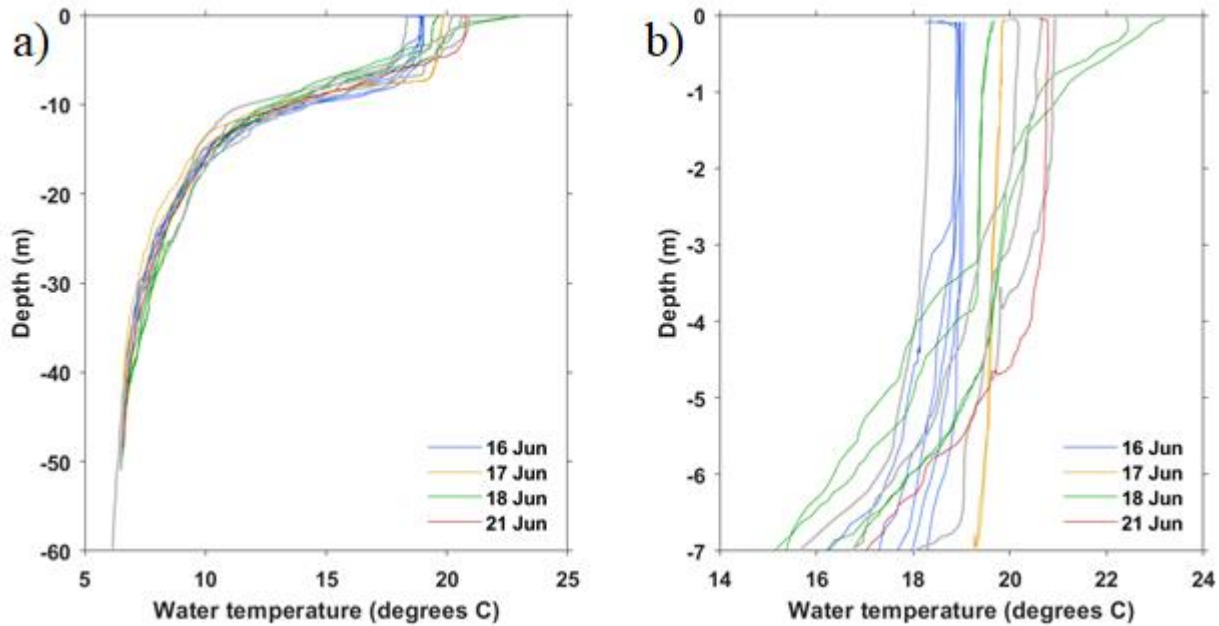
Figure 6. (a) Vertical temperature profiles in lake water for different days. The thermocline is located between about 7 to 13 m depth. (b) Enlargement of the upper mixed layer section (0-7 m depth). Grey lines are profiles taken during 11, 13 and 19 June 2019.

4 Meteorological conditions during L-WAIVE

4.1 Synoptic conditions

During L-WAIVE, France was under the influence of two main synoptic features, namely a pronounced trough over Britany and the British Isles and a high-pressure ridge over north Africa, sometimes extending across the Mediterranean and all the way into eastern Europe. This weather situation is illustrated in Figs. 7 to 9 using the Fifth European Centre for Medium-Range Weather Forecasts Reanalysis (ERA5) at 0.75° horizontal resolution. This configuration caused a particularly strong pressure gradient over the western Mediterranean for the period 12-15 June (Fig. 7), flanked in the east by an intense Libyan anticyclone, transporting warm air from sub-tropics to mid-latitudes. The ridge weakened and broadened over the following days (16-19 June, Fig. 8) before strengthening again (20-23 June) as the Libyan high intensified (Fig. 9).

During the course of the campaign, the area of interest was under the influence of warmer temperatures in the free troposphere linked with the high-pressure ridge at the beginning and the end of the field campaign, and colder temperature from 20 to 22 June. Since the experiment was conducted in a valley, where ERA5 reanalyses are generally considered not to be very accurate below the average altitude of the mountains (~2 km a.m.s.l. in our case), it is more informative to use the measurements acquired during the field campaign from the lidar and ULAs to describe the evolution of meteorological variables (wind, humidity, temperature, pressure).
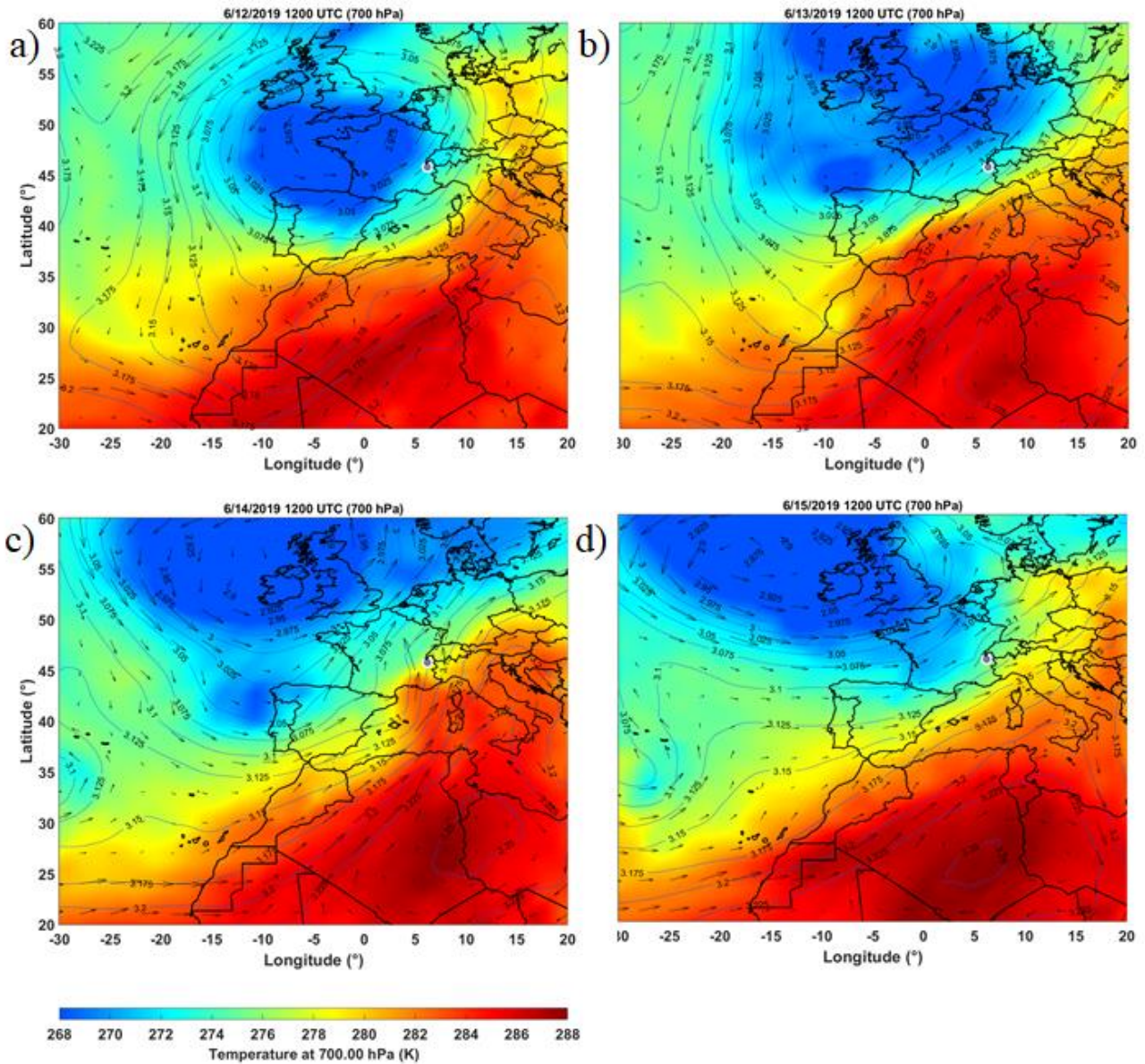
370   **Figure 7. ECMWF ERA5 temperature at 700 hPa (K, shading), geopotential height at 700 hPa (gpm/1000, contours) and horizontal winds at 700 hPa (black vectors) on (a) 12 June 2019 at 12 UTC, (b) 13 June 2019 at 12 UTC, (c) 14 June 2019 at 12 UTC, and (b) 15 June 2019 at 12 UTC. The location of Lathuile is indicated with a grey dot surrounded by white.**
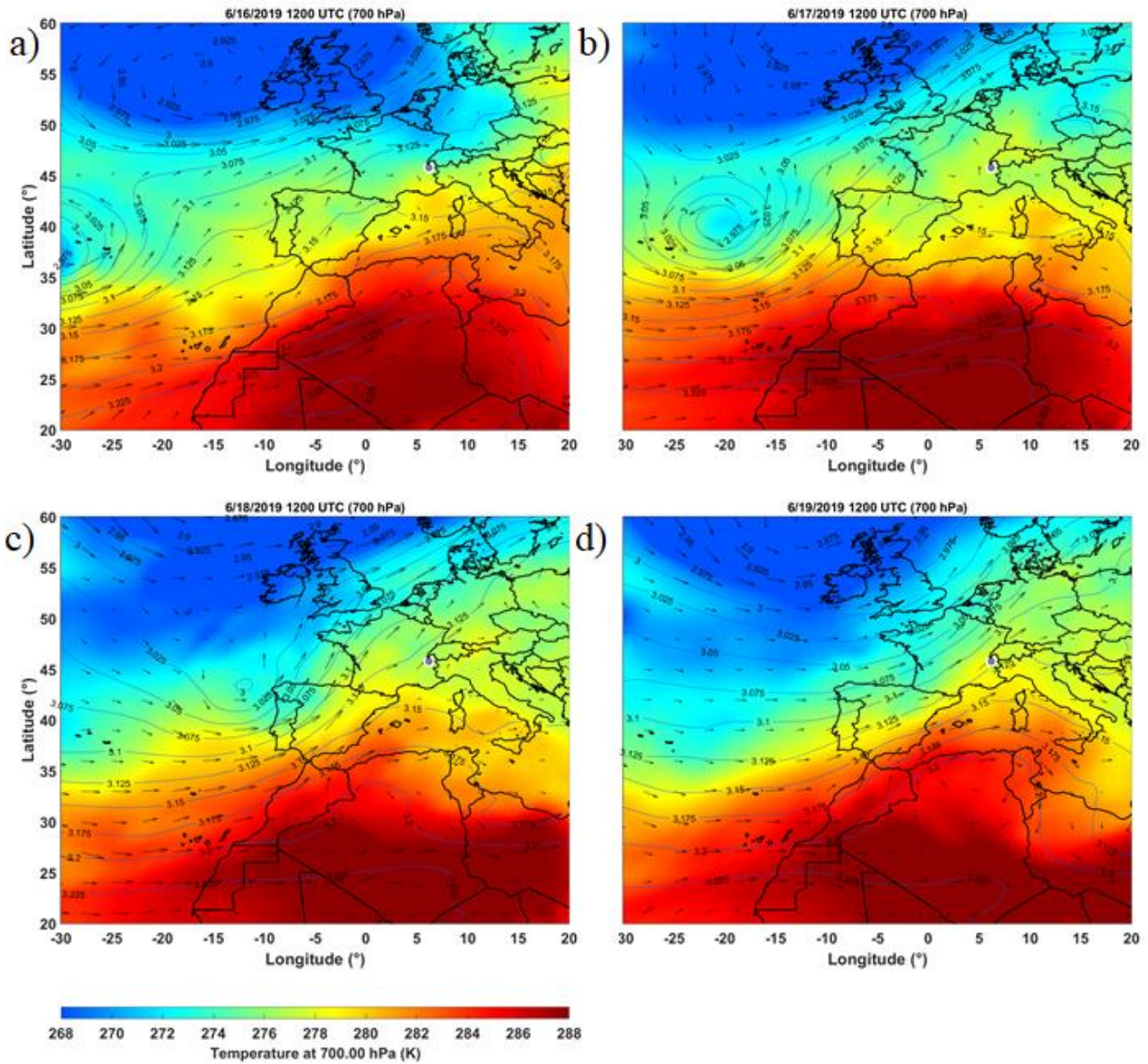
Figure 8. Same as Fig. 8, but for the period 16-19 June 2019.
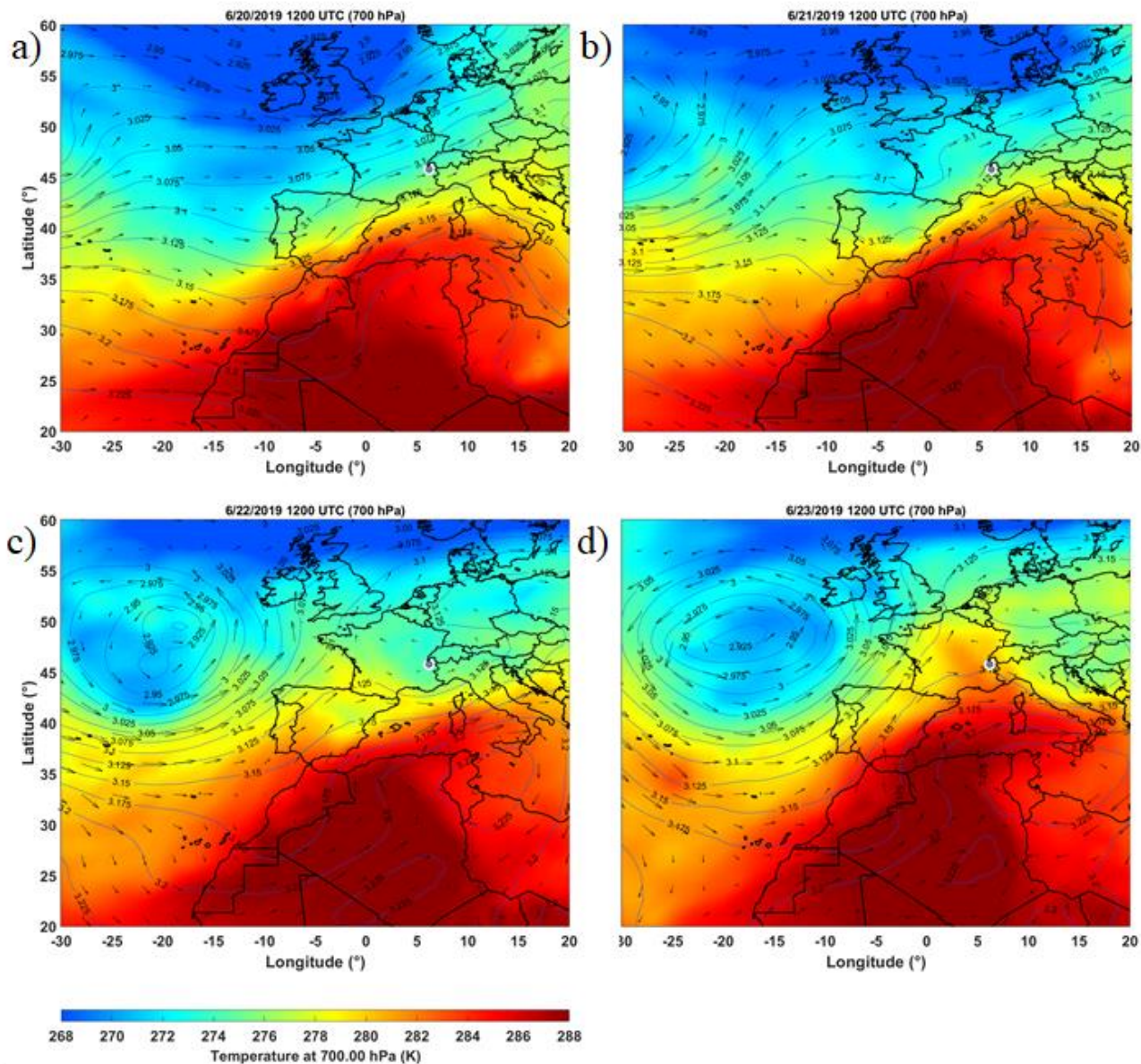
375

Figure 9. Same as Fig. 8, but for the period 20-23 June 2019.

4.2 Scattering layers as tracers of local atmospheric dynamics

Rayleigh-Mie lidars are very efficient tools to detect aerosol layers, but also clouds (e.g. Platt, 1977; Berthier et al., 2004), both semi-transparent (ice clouds) or opaque (liquid water clouds) to the laser beam. During L-WAIVE, the temporal evolution

380 of the aerosol burden and clouds above the Annecy lake have been monitored using both the ground-based lidar WALI and the airborne lidar ALiAS. In addition, continuous monitoring of aerosols vertical distribution from a lidar gives insight into air

masses transport. The identification of their particulate constituents (such as dust or pollution aerosols) may also provide information on the origin of observed air masses. For instance, such a capability was used to improve our understanding of atmospheric circulation in complex situations such as extreme heat wave phenomena (Chazette et al., 2017).

385 Fig. 10 shows the temporal evolution of the vertical profile of the aerosol scattering ratio (ASR, Fig. 11a) and of the linear volume depolarization ratio (VDR, Fig. 10b), as defined in Appendix E. It can be seen that the vertical extension of aerosols in the valley is highly variable over time as is the presence and nature of clouds during the course of the campaign. There is a strong diurnal cycle of ASR in the valley which is probably related to the slope winds. The depth of the aerosol layer is largest around 0000 LT when downslope winds tend to favour the accumulation of aerosols in the valley, while it is exhibiting a

390 minimum around 1200 LT when upslope wind tend to flush aerosols out of the valley. Moreover, significant day-to-day variations of the aerosol layer depth are observed with the lidar-derived ASR which highlights local, regional and synoptic scale transport of air masses over the Annecy valley. At the beginning of the campaign (mainly on 14 June) large VDR values are detected up to altitudes exceeding 7 km a.m.s.l. (Fig. 10b). These large VDR values are related to a large-scale Saharan dust transport episode over the Lac d'Annecy valley favoured by the synoptic conditions on that day (see Section 4). These

395 aerosols are progressively mixed downward by subsidence, reaching the valley floor around 0000 LT on 15 June. Slightly enhanced VDR values are also evident on 19 and 20 June that are associated with local and/or regional pollution advected at altitude and verticaly mixed by dry convection.

The period was rather cloudy as shown in Fig. 10a (shaded areas) where cloud types and the raining periods including thunderstorms are indicated. It is worth noting that large lidar-derived VDR values detected in the presence of dense clouds

400 are related to multiple scattering (areas appearing in pink in Fig. 10b), rather than the presence of non-spherical aerosols.

The measurements made with the airborne particle sizer corroborate the nature of the particles identified from the lidar observations. Figure 11 shows that on 14 June, larger particles are observed above 2.5 km a.m.s.l., compatible with the presence of dust-like particles in the lower troposphere. It should be noted that on 19 and 20 June, the mean radius of the particles does not exceed 0.4 µm, suggesting the presence of pollution aerosols mixed with some industrial dust-like particles explaining

405 enhanced VDR values. The altitude distribution of particle size on 19 and 20 June are also quite different, with large concentrations of small particles being observed from the surface to 4 km a.m.s.l. on 19 June indicating more efficient dry convection, whereas on 20 June, the largest particle concentrations are only observed below 2 km a.m.s.l.
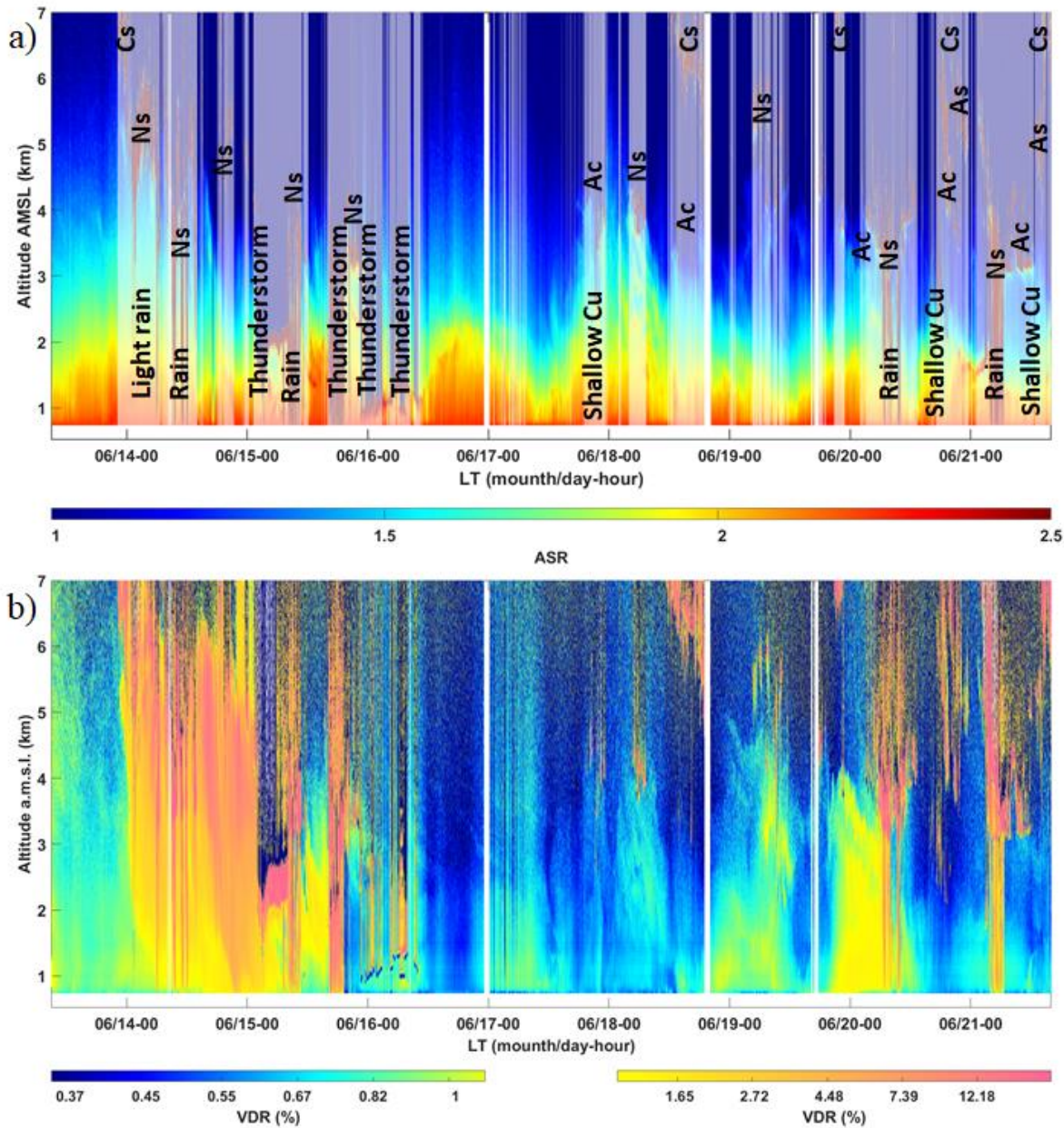
Figure 10. Temporal evolution of a) the aerosol scattering ratio (ASR) where the shaded areas correspond to the presence of clouds and b) the linear volume depolarization ratio (VDR) from 13 to 21 June 2019. The cloud type and rain location are indicated, as is the type of the main aerosol structures identified by the VDR (orange/pink for dust on 14 June and other for pollution aerosols, clouds are in pink). Cs, Ns, As, Ac and Cu indicate cirrus, nimbostratus, altostratus, altocumulus and cumulus clouds, respectively.
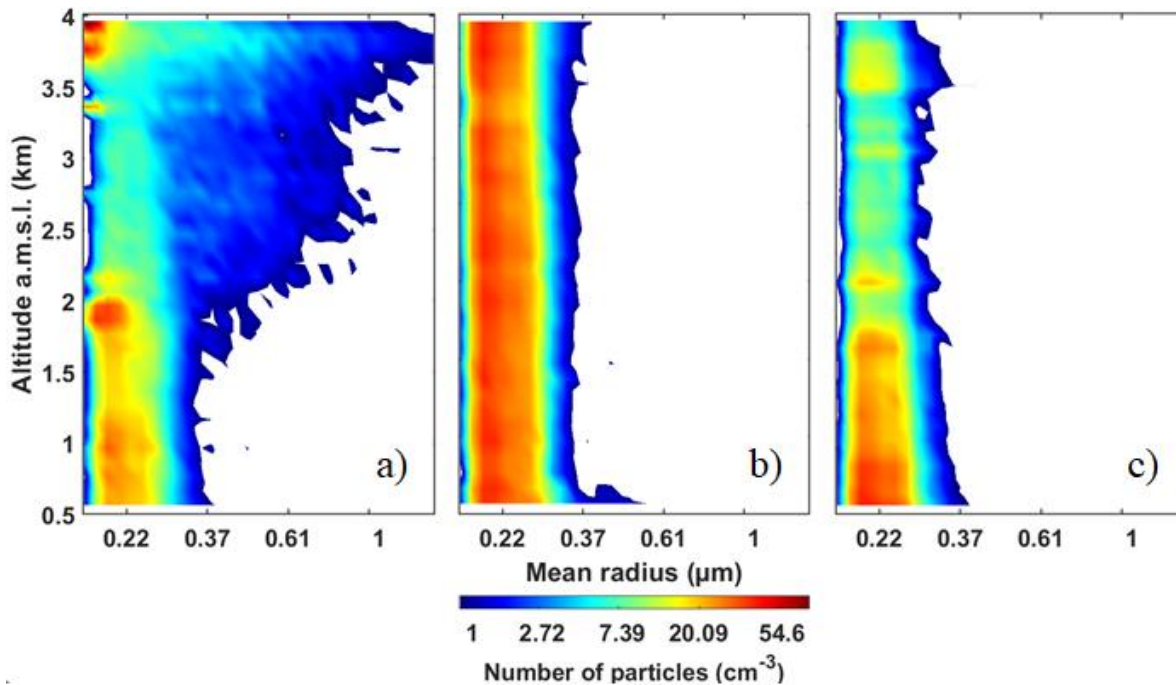
Figure 11. FIDAS-derived aerosol size distribution for the flights a) F05 on 14 June (long-range transport), b) F17 on 19 June (local pollution) and c) F18 on 20 June 2019 (regional pollution).

4.3   Local wind

The temporal changes in wind intensity and direction observed by wind lidar are given in Fig. 12. Weak winds, generally less than 5 ms^{-1}, are observed in the valley, below 2 km a.m.s.l. The wind intensity does not show repetitive patterns from one day to the next. In contrast, wind direction shows regular variations (Fig. 12b), with winds directed towards the exit of the valley (south) during the day, consistent with the flushing of aerosols suggested by the lidar observations. During the night, winds are directed towards the city of Annecy, thereby contributing to the accumulation of aerosols in the Annecy lake catchment. The local wind in the valley is obviously disturbed during stormy periods and during the episode of dust long-range transport on 14 June. The presence of these aerosols at higher altitudes (up to ~5 km a.m.s.l.) allowed the wind to be retrieved with the wind lidar above 2 km a.m.s.l. Strong southerly winds (in excess of 20 m s^{-1} above 3.5 km a.m.s.l.) were observed in agreement with the meteorological fields in Fig. 7b-c. The upper part of the regional pollution plume on 20 June is also seen to be associated with stronger southwesterly winds in excess of 10 m s^{-1} (Fig. 12a).
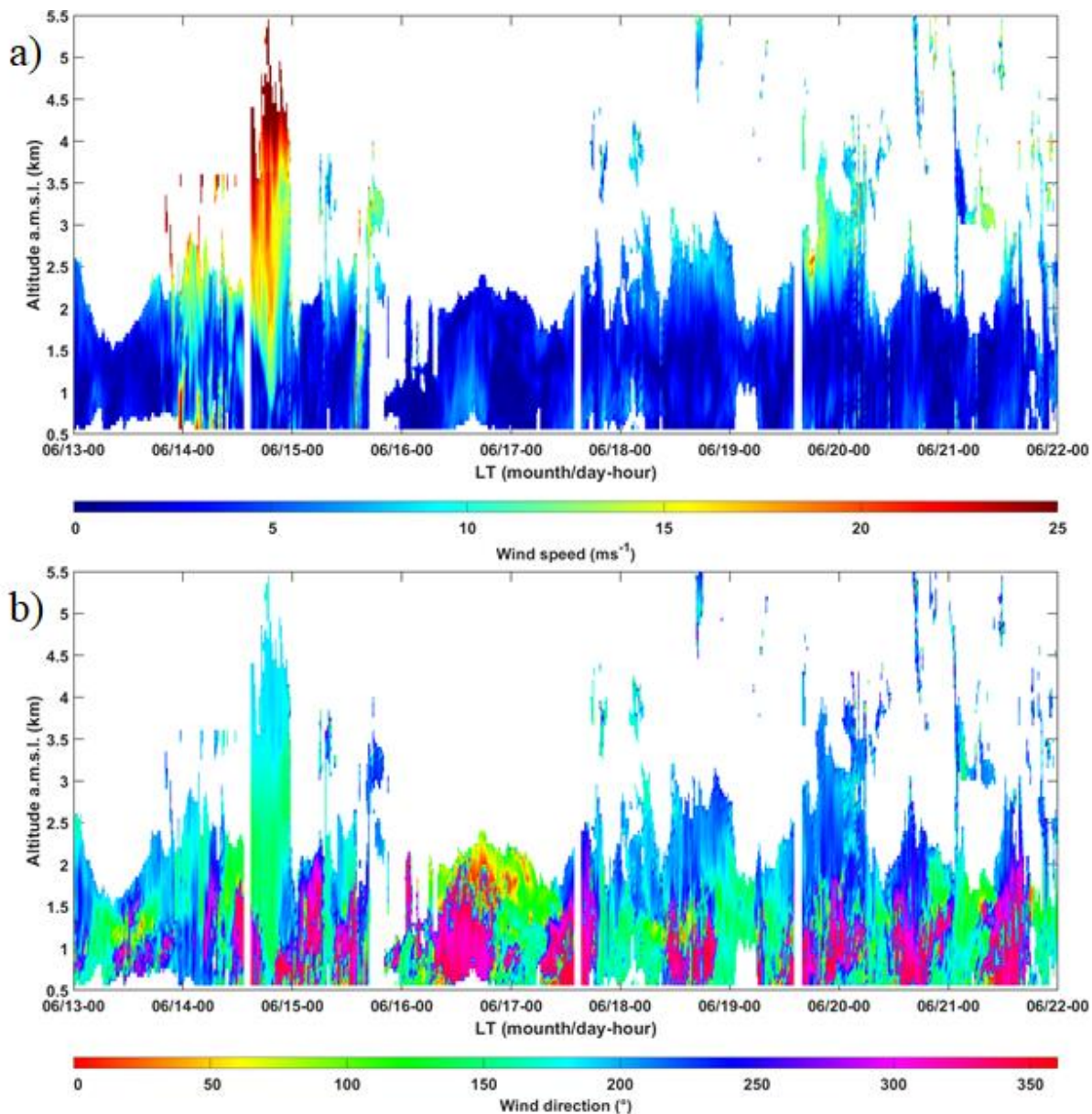
Figure 12. Temporal evolution of a) wind speed (m s^{-1}) and b) wind direction (0° is for North and 90° for east) obtained from wind lidar.

430 **5   Water vapor in the low troposphere during L-WAIVE**

Water in vapor phase was sampled throughout the campaign in terms of mixing ratio of the main isotope and abundance of isotopes $H_2^{18}O$ and $H^2H^{16}O$. At the same time, liquid water samples were taken from the surface of the lake, in the clouds, and

surface precipitation to obtain their isotopic contents, and to place them in the context of the atmospheric water vapor of the lower troposphere.

5.1 Ground-based lidar measurements and analysis

The vertical profiles of WVMR derived from the WALI ground-based lidar are shown in Fig. 13a. They show highly variable water vapor in the first 2 kilometers of the atmosphere. Lower WVMR values are associated with nighttime downslope winds for instance, and higher values are generally associated with upslope valley winds but may persist during days associated with heavy precipitation such as on 15 June 2019. When northerly winds prevail in the planetary boundary layer of the valley, air masses are advected along the lake axis before reaching the measurement site, resulting in an increase of water vapor associated with a probable evaporation of the surface water of the lake. The influence of the lake is thus seen mainly up to altitudes between ~1 and 2 km a.m.s.l. during the day and clearly lower the rest of the time ($\lesssim 0.5$ km a.m.s.l.), when the airflow comes mainly from the mountain tops (e.g. Brulfert et al., 2005).

Some of the marked WVMR features observed in the lidar measurements are reproduced in the high-resolution (0.25°) WVMR fields of ERA5 (Fig. 13b), especially during the second part of the campaign, starting on 18 June 2019. The more pronounced differences in the first part of the campaign are related to the large number of thunderstorms and strong rainy periods that are more difficult to grasp with ERA5. For instance, the boundaries between the different moist air mass types are similar in the lidar measurements and in the reanalyses, although the reanalyses are moister in the planetary boundary layer. There is a strong decrease of water vapor at altitude ~3 km a.m.s.l. which marks the transition to the free troposphere where long-range transport occurs. The altitude of this sharp transition exhibits a diurnal cycle and is mainly driven by the vertical stability of the lower troposphere. It is also influenced by the average altitude of the mountains surrounding the measurement site.
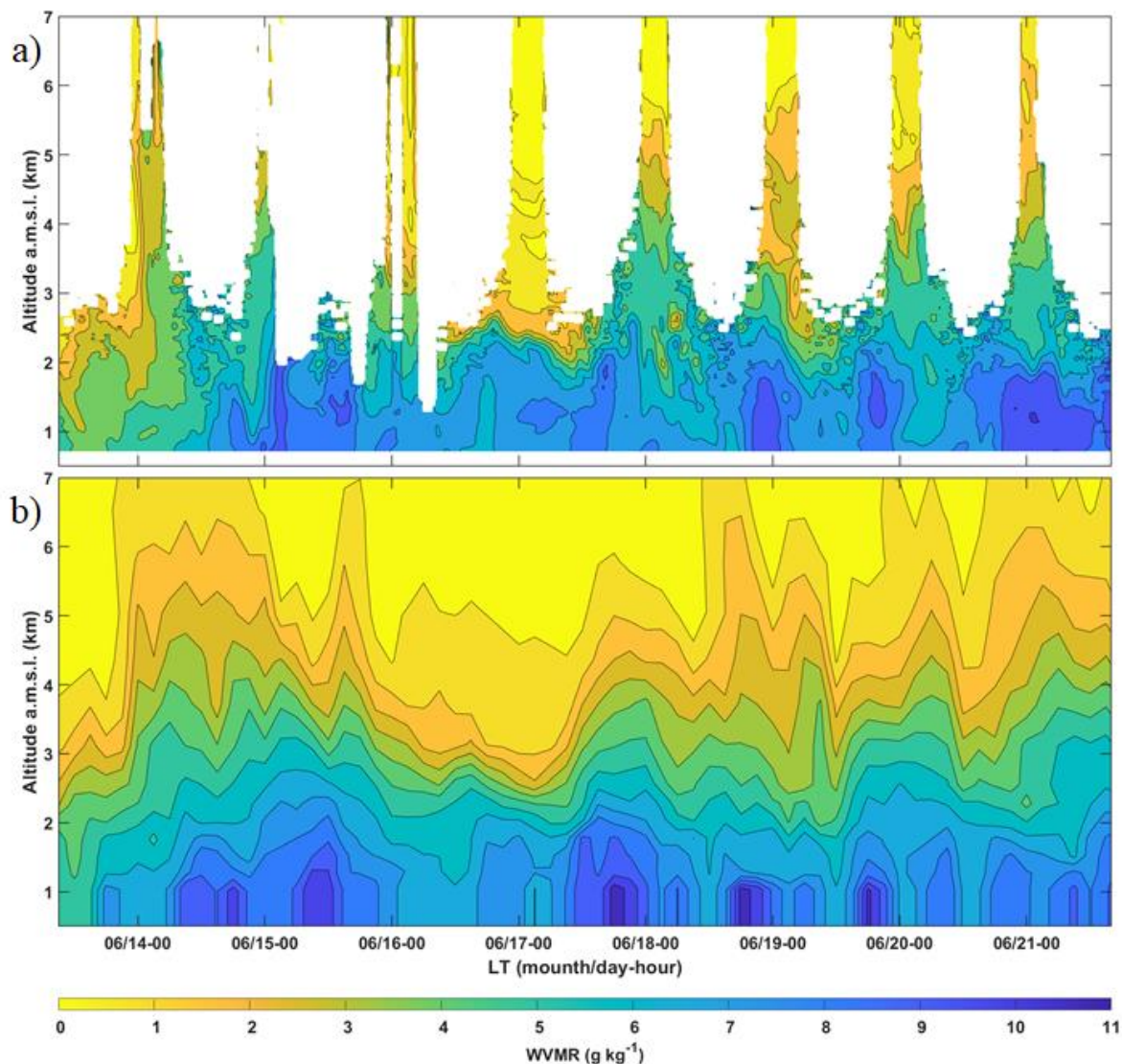
Figure 13: Temporal evolution of the water vapor mixing ratio (WVMR) derived from the ground-based Raman lidar and b) ERA5 reanalysis at 0.25° horizontal resolution from 14 to 21 June 2019 over Lathuile. White areas in a) correspond to missing data during the daytime above 2-3 km a.m.s.l. caused by detection limitations of the lidar.

5.2   Water isotope survey of the lake d'Annecy region

Stable isotope content of water vapor and in liquid water was quantified regarding $H_2^{18}O$ and $H^2H^{16}O$, as well as the deuterium excess (d-excess*). Water vapor was sampled in-situ using a CRDS, whereas liquid samples, including precipitation, cloud water and lake water were analysed in the laboratory. Here we report the isotope composition (see interpretative framework in Appendix C) as delta-values relative to a standard (e.g. Gat, 1996).

5.2.1 Atmospheric water vapor sampling

In total, 15 flights with ULA-IC have been performed (see Table B2) including 13 flights where the CRDS allowed a representative sampling of $\delta\,^2H$ and $\delta^{18}O$ (the analyzer was offset due to saturation throughout flight 11, and shorter segments in other flights, which are excluded in the present analysis, see Appendix D). The isotope content $\delta\,^2H$ observed during the flights ranged between about -340 and -80‰ for flight altitudes up to ~3.5 km a.m.s.l. as shown in Fig. 14a. For this figure, we considered ascending and level flight segments, and excluded rapid ascends with pressure increases larger than 1hPa/10s. As observed in earlier studies, the dataset is clustered along a typical mixing line in $\delta\,^2H - q$ space (Noone, 2012; Salmon et al., 2019; Sodemann et al., 2017). The end-members of the mixing lines show substantial day-to-day variations, from $\delta\,^2H=$-110 to -80‰ (~[-16, -12]‰ for $\delta^{18}O$, not shown) for the more humid end member (q > 8 g kg^{-1}), and from $\delta\,^2H=$-340 to -230‰ (~[-30, -20]‰ for $\delta^{18}O$, not shown) for the drier end member (q < 3 g kg^{-1}). It is important to keep in mind that both, the variation in maximum flight altitudes and the meteorological situation can contribute to variability.

As shown in Fig. 14b, the vertical profiles of the isotope content $\delta\,^2H$ seem rather uniform below 2 km (an impression also reinforced by the range of $\delta\,^2H$ values covered in the graph), and, in some cases, exhibit strong vertical gradients at higher elevations, as seen between 2.5 and 3.6 km a.m.s.l. during 4 flights (flights 5, 6, 9 and 10). The same patterns are observed on the vertical profiles of $\delta^{18}O$ (not shown) and even on the WVMR profiles derived from the meteorological probes onboard the 2 ULAs. The sharp gradients are not observed systematically, as in the case of flight 15 (20 June), or they are present at a higher altitude, not sampled by the flight.

These strong gradients in altitude are related to the transition to the free troposphere, and are confirmed by the lidar observations and meteorological measurements on the two ULAs. The observed vertical gradients in isotope ratios evolved as a function of the different isotope composition of boundary layer vapor, free-troposphere vapor, and the stratification in the lower troposphere above the valley which depends on the meteorology (as for example rainy events) but also on the time of day when the flights were made. In the early afternoon, the boundary layer is shallower and less buoyant, leading to a transition at lower altitude (flights 5 and 6). Flights 5 and 6 also took place in the aftermath of heavy thunderstorms occurring in the morning of 16 June that led to a cooling of the surface. In the late afternoon, thermal convection is generally more efficient, and the transition may occur at higher altitudes (flight 10 on 18 June 1700 LT). Flight 9 on 18 June 1200 LT does not seem to follow the same rule. As shown in the vertical lidar profiles in Fig. 10, the clouds around 4 km a.m.s.l. seem to exert a forcing on the boundary layer which moves its top to higher altitudes (~3.5 km a.m.s.l.).

Because of the cloud cover and depending on the wind conditions, ULAs have not been able to fly in the free troposphere on most days. However, this was possible for flight 10 where a marked reduction of $\delta\,^2H$ occurred just above 3 km a.m.s.l., while higher values of isotopic content are seen at higher altitudes that match those below the transition. The same behavior was observed on independent measurements of water vapor mixing ratio, which suggests filamentation associated with

differential transport of drier air layer. This type of conclusion cannot be drawn for the other days due to the maximum flight altitude reached.
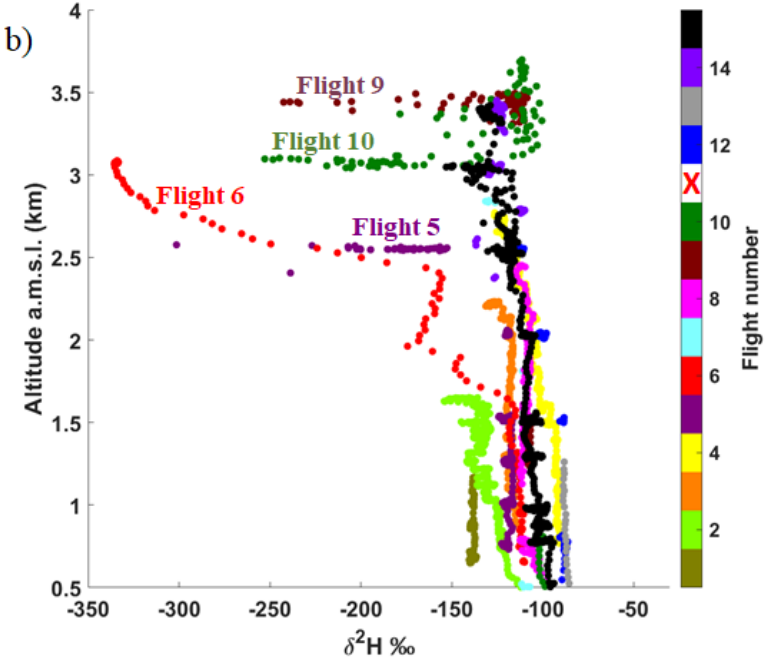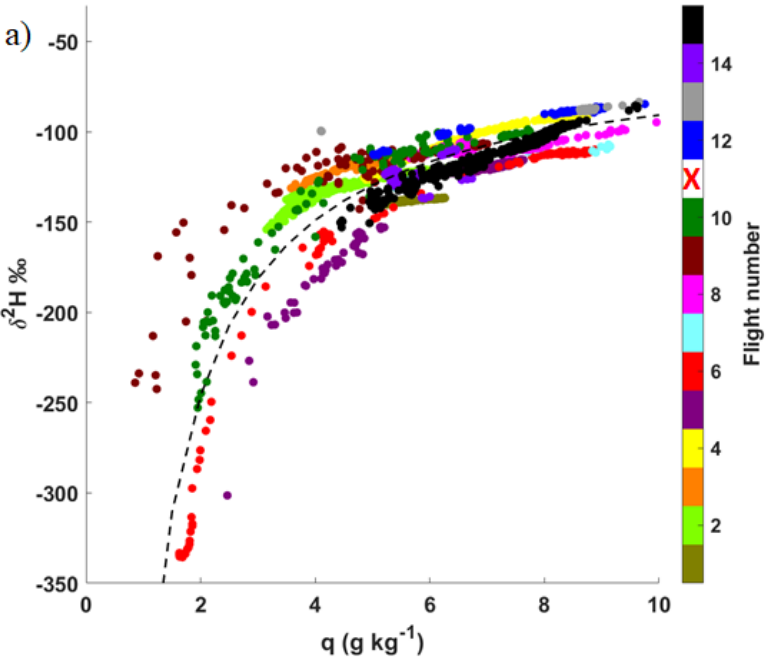
495 **Figure 14. Overview of airborne water vapor isotope measurements. (a) Isotope content $\delta\,^2H$ (permil) vs. specific humidity (g kg-1). The mean mixing lines is computed following Noone (2012) and reported using a black dotted line. (b) Vertical profiles of $\delta\,^2H$ (‰). Color indicates flight number. Isotope data are averaged at 10s interval. The red cross associated with Flight 11 indicates that no data was relevant during that flight.**

500 ### 5.2.2   Cloud liquid water sampling

Four relevant cloud water samples have been taken with the CASCC on 18, 20 and 21 June (Table A1). The isotope contents of the cloud water samples are shown in Fig. 15a (coloured circles). They are close to the global meteoric water line (GMWL) with corresponding d-excess values ranging from 12.1 to 14.8 ‰. Equilibrium condensates were estimated from relevant water vapor isotope measurements during the time when the cloud samples were taken (Fig. 15a, coloured squares) using the

505 fractionation factors of Majoube (1971), and air temperature measurements at cloud level, ranging between -4 and 1°C. It is worth noting that given potential sources of uncertainty, the equilibrium condensate values agree remarkably well with the cloud water samples during 18 June (green symbols), and the afternoon of 20 June (violet symbols). Overall, results here confirm that the cloud water formed from equilibrium fractionation from ambient vapor. It is worth mentioning that such agreement between the completely independent sampling and measurement of vapor and cloud water supports the overall

510 validity of i) the cloud water sampling protocol, ii) the airborne vapor isotope measurements and iii) the consistency of the calibrated water isotope dataset derived from the L-WAIVE campaign.
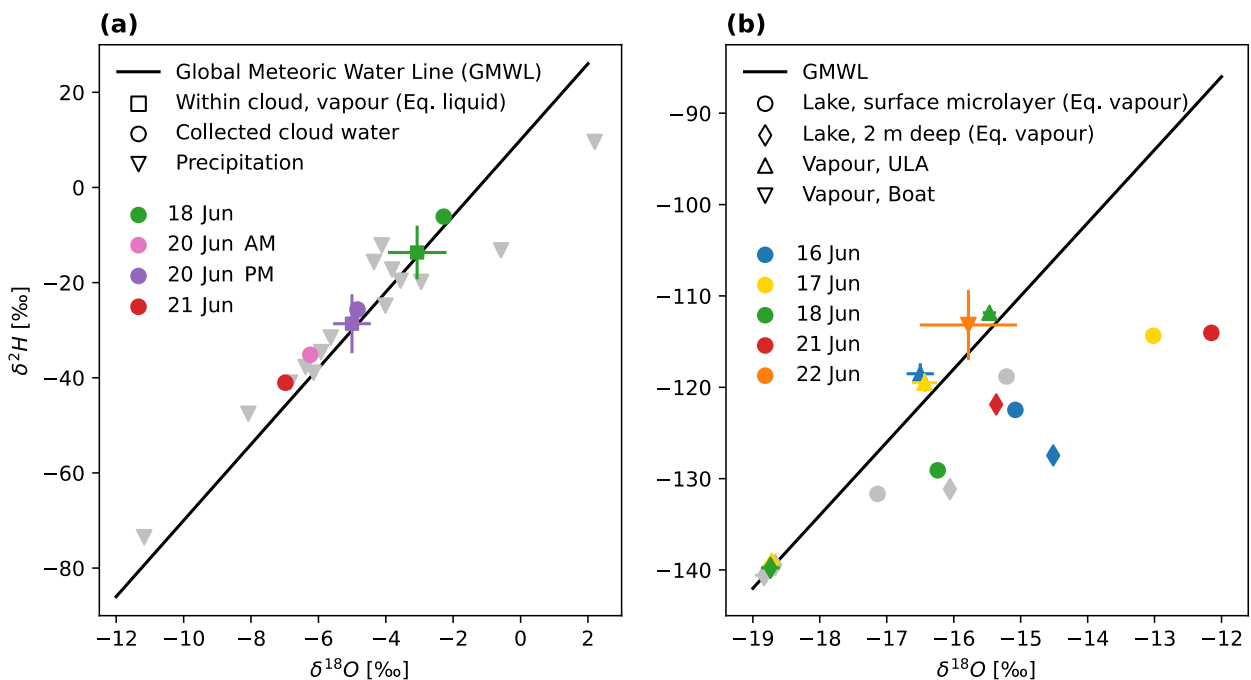
Figure 15. δ^2H - $\delta^{18}O$ **plots of liquid samples with the vapor isotope estimates. (a) Cloud water samples (circles), equilibrium condensate (squares), and precipitation samples (grey triangles). (b) Equilibrium vapor from lake water samples at different depth (dots and diamonds) compared to vapor isotope measurements from ULA-IC (upward triangle) and boat (downward triangle). Colour denotes matching dates. Gray colours show data where the vapor samplings are not available. Black line denotes the Global Meteoric Water Line (GMWL).**

5.2.3 Precipitation sampling

In total, 28 precipitation samples, of which 22 are unique, have been taken during the campaign, with sampling times lasting from 20 min to several hours, depending on rainfall rate (Table A1). The isotope composition in rainfall ranges from -11.2 to 2.2‰ in $\delta^{18}O$ and -73.5 to 9.6 ‰ in δ^2H (Fig. 15a, grey triangles), with corresponding values of d-excess between 3.5 and 20.8‰ (not shown). Even if evaporation effects from the sampling setup cannot be fully excluded, in particular for the samples with a sampling duration of more than 3h, the consistency of duplicate samples indicate that the influence of sampling artefacts can overall be considered as limited. Notably, there is an overall correspondence between the isotope range observed in cloud water samples and in a majority of precipitation samples. Deviations of precipitation samples from the GMWL indicate potential below-cloud exchange processes between the falling raindrops and the ambient water vapor, leading to an enrichment of the precipitation in ^{18}O (Graf et al., 2019; Worden et al., 2007). Samples taken between 12 to 15 June, and on 21 June are most enriched in ^{18}O, exhibiting higher values in $\delta^{18}O$ and δ^2H and a smaller d-excess. These samples are from rainfall events associated with local thunderstorms (see Fig. 11a). The low d-excess (even negative, ~-8‰) of these samples may point to the partial evaporation of rain droplets during their fall.

5.2.4 Lake liquid water sampling

Evaporation from the Annecy lake is expected to be an important source for the water vapor in the Annecy valley. In order to link the atmospheric profiles of water vapor isotopes to the lake as a moisture source, 20 lake water samples (Table A1) were taken throughout the campaign within the lake-atmosphere interface layer (6 samples), as well as close to 2 m depth (14 samples), and analysed for their stable water isotope composition. The average isotope contents were -8.3±1.5‰ for $\delta^{18}O$, and -63.0±6.0‰ for δ^2H. The equilibrium vapor from these liquid samples (Fig. 15b) allows to compare to vapor measurements (see below), while leaving the d-excess unaffected. Lake water samples taken close to the surface are expected to be most affected by evaporation, causing deviations to the right from the GMWL along evaporation lines (enrichment in ^{18}O), and corresponding to a negative d-excess. This deviation is clearly observed in Fig. 15b for the majority of equilibrium vapor from the lake water samples. The corresponding d-excess underline this result for the 6 lake water samples from the lake-atmosphere interface layer, with values of the d-excess ranging between 2.2 and -19.6‰ and an average value of -6.3‰. For the samples taken at a depth of 2 m (Fig. 15b, diamond symbols), the derived d-excess showed less evaporation influence, with a mean of 0.6‰, and a standard deviation of 8.2‰. While some sampling artifacts cannot be fully excluded, the fact that there are differences between the isotope contents at the interface and 2 m depth points to the impact of ongoing evaporation, that decreases towards a depth of 2 m. Indeed, temperature profiles taken within the lake show a typically strong, but variable

thermocline below about 7 m depth during the campaign (Fig. 6a). Therefore, freshwater input from runoff and precipitation, and loss to evaporation are expected to primarily affect the warmer, upper mixed layer within the timeframe of the campaign.

To assess the isotopic balance between the lake water and the water vapor isotope composition measured by ULA and boat, we calculated the equilibrium vapor for the lake surface temperatures measured during respective days (Fig. 6b) using the equilibrium fractionation factors of Majoube (1971). Lake water samples clearly cluster on the right-hand side of the GMWL (Fig. 15b, diamonds), whereas vapor data from the ULA-IC (triangles) and the boat (downward triangle) are to the left, with a relatively consistent range of isotope values. The range of equilibrium vapor for δ^2H observed in lake water for 16 and 17 June (Fig. 15b, blue and yellow dots) matches to first order with the range of δ^2H from ULA-IC. The $\delta^{18}O$ in equilibrium vapor, however, has substantially higher of $\delta^{18}O$, in agreement with expectations for kinetic (non-equilibrium) fractionation during lake evaporation. During both 18 and 22 June (Fig. 15b, green and orange dots), equilibrium vapor of the liquid samples has a lower heavy isotope content than observed by ULA-IC, pointing to the influence of other factors on either atmospheric or lake water composition on these days. It is worth noting that Lake Annecy is fed by a catchment whose surface is 10 times larger than that of the lake via ten main tributaries located on the lake periphery. The flows of its tributaries increase significantly in situations of heavy rain, which can substantially influence the isotopic content of the lake during the course of a year.

5.2.5 Synthesis and discussion

The main atmospheric vertical structures are derived from the vertical profiles of potential temperature, aerosols, wind and RH. For the illustration, Fig. 16 shows a typical vertical RH profile that highlights the different layers present between the lake (~0.5 km a.m.s.l.) and about 4 km a.m.s.l.: the lake boundary layer (LBL) between ground level and ~1 km a.m.s.l. (layer 1), the layer defined by the lake region of influence (LRI) located between about 1 and 2.5 km a.m.s.l. influenced by the area of the lake surrounded by mountains about 2 km high on its southern part (layer 2), a transition towards the free troposphere between ~2.5 and 3.5 km, influenced by the regional circulation (layer 3) and above ~3.5 km a.m.s.l. the free troposphere with a synoptic influence, where long-ranged transport of air masses may occur. The location in altitude of these different layers obviously depends on the weather conditions and the time of day.

Using the vertical layering introduced above, the overall results for stable isotopes in water are summarized in Fig. 17 on a statistical basis. This synthesis is presented in the form of whisker boxes for d-excess (Fig. 17a), δ^2H (Fig. 17b) and $\delta^{18}O$ (Fig. 17c). For each sub-figure, the upper part depicted the statistical content of isotope in water vapor for each sampled altitude range in the atmosphere, while the lower part describes the same thing for samples collected in the depth of the lake. For each whisker box, the central continuous vertical line indicates the median (50th percentile, P_{50}), and the bottom and top edges of the box indicate the 25th (P_{25}) and 75th (P_{75}) percentiles, respectively. The whiskers extend to the most extreme data points not considered outliers, which are values outside the interval bounded by the 5th and 95th percentiles.

For the atmospheric water vapor, the sample number n is significant (numbers given at the right of the whisker boxes in Fig. 18b) and it makes sense to accurately assess the confidence interval at 95% defined by $\left[\left(P_{50} - 1.57 \cdot (P_{75} - P_{25})/\sqrt{n}\right)\left(P_{50} + 1.57 \cdot (P_{75} - P_{25})/\sqrt{n}\right)\right]$. The notches in the upper part of the sub-figure represent this confidence interval. As they do not overlap from an atmospheric layer to another, we can conclude, with 95% confidence, that the true medians do differ. Hence, we highlight a significant variability in the stable isotope content of water vapor depending on the atmospheric layers previously identified.

Between the surface of the lake and 2.5 km a.m.s.l., we find $\delta^{18}O$ values are in the lower range to those recorded by Craig and Gordon (1965) for evaporation over the Mediterranean [-15,-10] ‰. On the other hand, they report much more dispersed d-excess values ranging from 5 to 35‰. Gat (2000) gives narrower values for marine and European air masses with a d-excess interval of [7-11] ‰. Our observations are mainly outside this interval for the first two layers, they overlap it for the 2.5-3.5 km a.m.s.l. layer more influenced by the synoptic scale. Measurements from the boat on the last day of the campaign within 1 m above the lake are overall consistent with the vapor isotope measurements made by ULA-IC on previous days in the lake boundary layer.

Based only on the statistical information content provided by the whisker boxes profiles, it is difficult to see precisely whether the evaporation of lake water significantly influences the first layers of atmosphere just above the lake. Indeed, different factors can influence the relation between water vapor measured by the ULA above the lake, and the evaporating water vapor. In addition to the immediate evaporate, water vapor can be advected and mixed in from other locations horizontally, but also vertically. In particular for a lake with coastal, vegetated areas within less than about 2 km distance anywhere on the lake, influences from evapotranspiration are likely within the lower 1 km above the lake. Since one would in steady state expect vapor without fractionation to derive from evapotranspiration (e.g. Gat, 1996), one would expect such a contribution to enhance variability in water vapor isotopes towards lower values of the d-excess.

Our liquid water samples are not numerous enough to define a confidence interval. As explained previously, we nevertheless note an enrichment in heavy isotope of the surface layer of the lake which is directly in contact with the atmosphere and therefore directly subject to evaporation. The 2 m depth layer is significantly less enriched as evidenced by their isotope content. We highlight therefore a significant enrichment in heavy isotopes of surface water associated with low values of d-excess, which is characteristic of evaporation as described by Gibson and Edwards (2002). Measurements of $\delta^{18}O$ profiles in the Annecy lake have already been carried out between the years 2000 and 2002. They have shown $\delta^{18}O$ values of the order of -9.5‰ for water above the thermocline of "Petit Lac" during the summer months (Danis, 2009), in agreement with our results. This indicates a year-to-year stability of the isotopic content of the lake water below the surface microlayer.

From a first analysis of our successful airborne in-situ sampling of water vapor isotopes and cloud water, we conclude that cloud water formed in an equilibrium fractionation process for the samples collected here, and the cloud water isotopes were relatively similar to local precipitation (taken on other days). Since 1992, the Global Network of Isotopes in Precipitation

(GNIP, https://nucleus.iaea.org/wiser) regularly sample rainwater at the Thonon-les-Bains city (60 km northeast from Annecy)

610 for isotope analyses. Based on data available until 2018, typical summer $\delta^{18}O$ ($\delta\ ^2H$) values fall within the interval [-16, -1] ‰ ([-120, -20] ‰), encompassing our precipitation and cloud water measurements. It should be noted that the lake water is poorer in heavy isotopes than rain and cloud water. This difference is probably due to snowmelt during spring and the contribution of precipitation falling at high altitude. Note that GNIP data show median values of -10.5‰ (-78.6‰) for $\delta^{18}O$ ($\delta\ ^2H$) during winter versus -6.5‰ (-43.5‰) during summer which agree with the studies of Dutton et al. (2005) and, Kendall

615 and Coplen (2001).
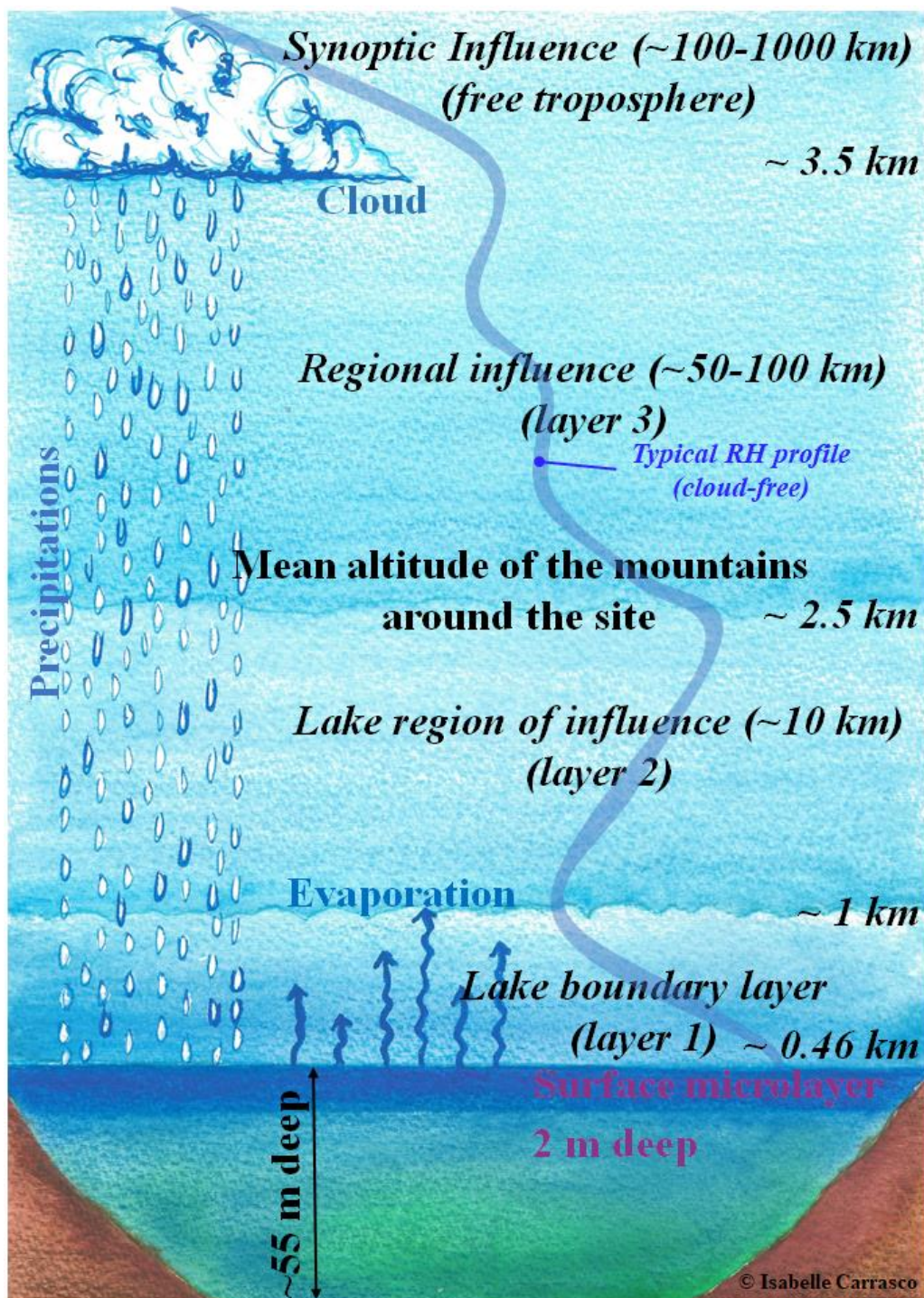
Figure 16. Schematic representation of the vertical structuring of the lower troposphere above the "Petit lac d'Annecy". The environments where gaseous and liquid water samples have been taken are highlighted. A typical vertical profile of atmospheric relative humidity is reported.
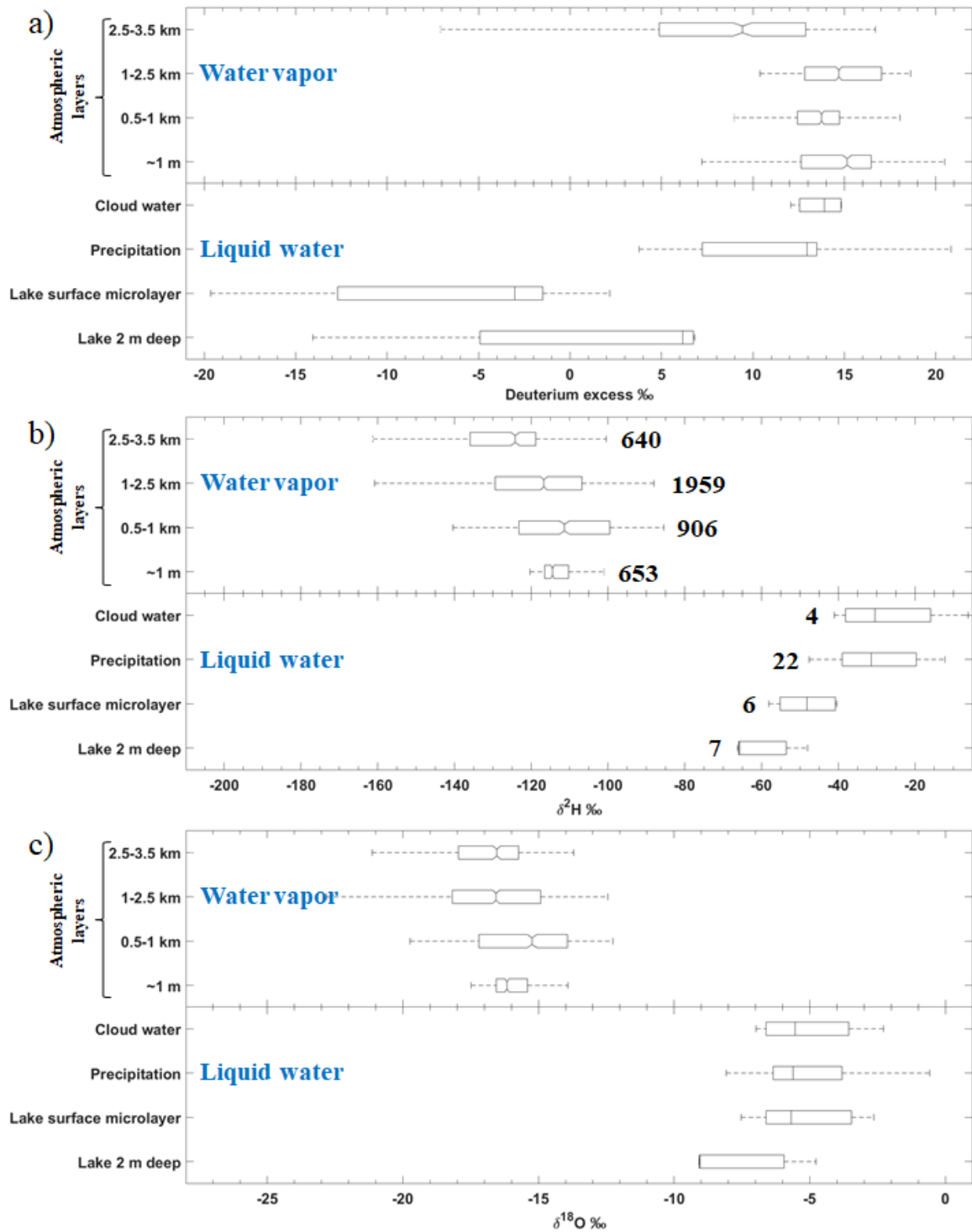
620

Figure 17. Whisker boxes for a) d-excess, b) $\delta\,^2H$ and c) $\delta^{18}O$. For each sub-figure, the upper part depicted the statistical content of isotope in water vapor and the bottom part in the liquid water.

6   Conclusion

An overview of measurements acquired during the field campaign L-WAIVE, as well as first research highlights, have been presented. Within L-WAIVE, we have developed an innovative approach to study evaporation processes and their heterogeneity over the Annecy lake in a variety of meteorological situations. The field campaign took place between 12 and 23 June 2019 and used the complementary and/or synergistic measurements from different means of sampling gaseous and liquid water. Continuous high vertical resolution profiling of tropospheric water vapor, temperature, and wind as well as aerosols in the Annecy valley have been performed. They are recorded together with boat-borne and airborne measurements of stable water isotopes (H_2O, H^2HO and $H_2^{18}O$) in the lake, in the lower atmosphere as well as in precipitation and and in-cloud using an original sampling method from ULA. Future ULA deployments of a CRDS analyser should take additional care on shielding from ambient temperature variations and condensation on the inlet to increase data yield.

The spatio-temporal evolution of the vertical profiles of WVMR appear coherent between the lidar retrievals and the ERA5 reanalysis, as well as with the measurements of the meteorological probes on board the ULAs. A marked diurnal cycle is observed with maximum WVMRs during the day (between 8 and 11 g kg^{-1}) when the valley winds are advected above the lake before reaching the measurement site. A significant temporal variability of the isotopic composition was observed within the first 1.5 km above ground level (a layer defined as the lake region of influence, below the average height of the mountains surrounding the lake) depending on weather conditions, as well as local and synoptic atmospheric circulations. We highlight that fairly well-mixed conditions prevailed in the lower free troposphere, between the lake surface and the 1.5 km of atmosphere above it. Strong vertical gradients in isotopes abundance were also observed at higher elevations, with a marked decrease at the interface with the free troposphere. The altitude at which these gradients were observed exhibited day-to-day variation throughout the measurement campaign in relationship with stratification in the valley, weather conditions, and topography. We note that the cloud water samples are close to the GMWL, (d-excess between 12.1 and 14.8 ‰), which indicates that the cloud water formed from equilibrium fractionation of ambient atmospheric water vapor. There is an overall correspondence between the isotope range observed in cloud water samples and a majority of precipitation samples (d-excess between -8.6 and 20.8/‰). The deviations observed on precipitation samples that are below the GMWL indicate potential below-cloud exchange, or post-condensational exchange processes. The average isotope composition of the lake water, taken at 2 m depth appears different from the one for the surface microlayer sample, due to evaporation processes. Moreover, the $\delta^{18}O$ in equilibrium condensate above the lake is generally substantially more depleted, confirming the existence of non-equilibrium fractionation during lake evaporation. It is worth noting that during 18 and 22 June, equilibrium vapor contained less stable isotopes than the atmospheric vapor, pointing to the influence of other factors on the water isotope composition above and within the lake.

Beyond the value of the dataset from L-WAIVE for satellite remote sensing validation, such as the Sentinel-5P satellite (https://sentinel.esa.int/web/sentinel/missions/sentinel-5p), similar experiments will be useful to test the dynamic range and resolution of H^2HO by remote sensing instrumentation, including ground-based and space-borne lidars.

Author contributions. Patrick Chazette coordinated the field campaign and wrote the paper, with contributions from Cyrille Flamant, Harald Sodemann, Anne Monod, Elsa Dieudonné and Julien Totems. Harald Sodemann and Andrew Seidl sampled and processed the stable water isotope data. Julien Totems calibrated WALI and derived the water vapor profiles. Patrick Chazette, Harald Sodemann, Julien Totems, Anne Monod, Elsa Dieudonné, Alexandre Baron, Andrew Seidl, Pascal Doira, Amandine Durand, and Sylvain Ravier participated in the field campaign. Hans Christian Steen-Larsen and all the authors contributed to proofreading of the paper.

Competing interests. The authors declare that they have no conflict of interest.

Acknowledgments. Friendly acknowledgements to local authorities of the town of Lathuile R. Aumaître, H. Bourne, F. Lambert; instrument providers F. Arthoud (USMB); D. Crucciani for its welcome at the Delta Evasion airfield; ULA pilots F., L., F. Toussaint; technical assistance F. Maignan and C. Diana. This research was funded by the WaVIL project (WAter Vapor and Isotope Lidar, Agence Nationale de la Recherche grant n°ANR-16-CE01-0009). HS and AS received funding from the Research Council of Norway with the FARLAB project (Contract no. 245907) and the ERC-2017-CoG ISLAS (Grant Agreement Nr. 773245). The IAEA/WMO Global Network of Isotopes in Precipitation (GNIP) is acknowledged for the access to its database accessible at: https://nucleus.iaea.org/wiser.

References

Barthlott, C., Corsmeier, U., Meißner, C., Braun, F. and Kottmeier, C.: The influence of mesoscale circulation systems on triggering convective cells over complex terrain, Atmos. Res., 81(2), 150–175, doi:10.1016/j.atmosres.2005.11.010, 2006.

Behrendt, A.: Temperature Measurements with Lidar, in Lidar., 2006.

Berkelhammer, M., Noone, D. C., Wong, T. E., Burns, S. P., Knowles, J. F., Kaushik, A., Blanken, P. D. and Williams, M. W.: Convergent approaches to determine an ecosystem's transpiration fraction, Global Biogeochem. Cycles, 30(6), 933–951, doi:10.1002/2016GB005392, 2016.

Berthier, S., Pelon, J., Chazette, P., Couvert, P., Sèze, G., Bréon, F.-M., Laland, M., Winker, D. and Pain, T.: Cloud statistics from spaceborne backscatter lidar data analysis, in European Space Agency, (Special Publication) ESA SP, vol. 2., 2004.

Bradley, S., Strehz, A. and Emeis, S.: Remote sensing winds in complex terrain - a review, in Meteorologische Zeitschrift, vol. 24, pp. 547–555, Schweizerbart'sche Verlagsbuchhandlung., 2015.

Brulfert, G., Chemel, C., Chaxel, E. and Chollet, J. P.: Modelling photochemistry in alpine valleys, Atmos. Chem. Phys., 5(9), 2341–2355, doi:10.5194/acp-5-2341-2005, 2005.

Chazette, P. and Totems, J.: Mini N2-Raman Lidar onboard ultra-light aircraft for aerosol measurements: Demonstration and extrapolation, Remote Sens., 9(12), doi:10.3390/rs9121226, 2017.

Chazette, P., Couvert, P., Randriamiarisoa, H., Sanak, J., Bonsang, B., Moral, P., Berthier, S. S., Salanave, S. and Toussaint, F.: Three-dimensional survey of pollution during winter in French Alps valleys, Atmos. Environ., 39(6), 1035–1047, doi:10.1016/j.atmosenv.2004.10.014, 2005.

Chazette, P., Sanak, J. and Dulac, F.: New approach for aerosol profiling with a lidar onboard an ultralight aircraft: application to the African Monsoon Multidisciplinary Analysis., Environ. Sci. Technol., 41(24), 8335–8341, doi:10.1021/es070343y, 2007.

Chazette, P., Dabas, a., Sanak, J., Lardier, M. and Royer, P.: French airborne lidar measurements for Eyjafjallajökull ash plume survey, Atmos. Chem. Phys., 12(15), 7059–7072, doi:10.5194/acp-12-7059-2012, 2012.

Chazette, P., Marnas, F. and Totems, J.: The mobile Water vapor Aerosol Raman LIdar and its implication in the framework

695   of the HyMeX and ChArMEx programs: application to a dust transport process, Atmos. Meas. Tech., 7(6), 1629–1647, doi:10.5194/amt-7-1629-2014, 2014.

Chazette, P., Totems, J. and Shang, X.: Atmospheric aerosol variability above the Paris Area during the 2015 heat wave - Comparison with the 2003 and 2006 heat waves, Atmos. Environ., 170, 216–233, doi:10.1016/j.atmosenv.2017.09.055, 2017.

700   Chazette, P., Totems, J., Baron, A., Flamant, C. and Bony, S.: Trade-wind clouds and aerosols characterized by airborne horizontal lidar measurements during the EUREC4A field campaign, Earth Syst. Sci. Data, 12(4), 2919–2936, doi:10.5194/essd-12-2919-2020, 2020.

Craig, H. and Gordon, L. I.: Deuterium and oxygen 18 variations in the ocean and the marine atmosphere. In Stable Isotopes in Oceanographic Studies and Paleotemperatures, edited by E. Tongiorgi, Laboratorio di Geologia Nucleare, Pisa., 1965.

705   Cui, B. L., Li, X. Y. and Wei, X. H.: Isotope and hydrochemistry reveal evolutionary processes of lake water in Qinghai Lake, J. Great Lakes Res., 42(3), 580–587, doi:10.1016/j.jglr.2016.02.007, 2016.

Cunliffe, M., Engel, A., Frka, S., Gašparović, B. Ž., Guitart, C., Murrell, J. C., Salter, M., Stolle, C., Upstill-Goddard, R. and Wurl, O.: Sea surface microlayers: A unified physicochemical and biological perspective of the air-ocean interface, Prog. Oceanogr., 109, 104–116, doi:10.1016/j.pocean.2012.08.004, 2013.

710   Danis, P.-A.: Modélisation du fonctionnement thermique , hydrologique et isotopique de systèmes lacustres : sensibilité aux changements climatiques et amélioration des reconstructions paléoclimatiques To cite this version : HAL Id : tel-00360067 Mod ´elisation du fonc, [online] Available from: https://tel.archives-ouvertes.fr/tel-00360067 (Accessed 5 November 2020), 2009.

Danis, P. A., Von Grafenstein, U. and Masson-Delmotte, V.: Sensitivity of deep lake temperature to past and future climatic
715   changes: A modeling study for Lac d'Annecy, France, and Ammersee, Germany, J. Geophys. Res. Atmos., 108(19), doi:10.1029/2003jd003595, 2003.

Dansgaard, W.: Stable isotopes in precipitation, Tellus, 16(4), 436–468, doi:10.3402/tellusa.v16i4.8993, 1964.

Drobinski, P., Steinacker, R., Richner, H., Baumann-Stanzer, K., Beffrey, G., Benech, B., Berger, H., Chimani, B., Dabas, A., Dorninger, M., Dürr, B., Flamant, C., Frioud, M., Furger, M., Gröhn, I., Gubser, S., Gutermann, T., Häberli, C., Häller-
720   Scharnhost, E., Jaubert, G., Lothon, M., Mitev, V., Pechinger, U., Piringer, M., Ratheiser, M., Ruffieux, D., Seiz, G., Spatzierer, M., Tschannett, S., Vogt, S., Werner, R. and Zängl, G.: Föhn in the Rhine Valley during MAP: A review of its multiscale dynamics in complex valley geometry, Q. J. R. Meteorol. Soc., 133(625), 897–916, doi:10.1002/qj.70, 2007.

Dutton, A., Wilkinson, B. H., Welker, J. M., Bowen, G. J. and Lohmann, K. C.: Spatial distribution and seasonal variation in
725   18O/16O of modern precipitation and river water across the conterminous USA, Hydrol. Process., 19(20), 4121–4146, doi:10.1002/hyp.5876, 2005.

Flamant, C., Drobinski, P., Nance, L., Banta, R., Darby, L., Dusek, J., Hardesty, M., Pelon, J. and Richard, E.: Gap flow in an Alpine valley during a shallow south fo¨hn event: Observations, numerical simulations and hydraulic analogue, Q. J. R. Meteorol. Soc., 128(582), 1173–1210, doi:10.1256/003590002320373256, 2002.

730   Gat, J. R.: Oxygen and hydrogen isotopes in the hydrologic cycle, Annu. Rev. Earth Planet. Sci., 24(1), 225–262, doi:10.1146/annurev.earth.24.1.225, 1996.

Gat, J. R.: Atmospheric water balance-the isotopic perspective, in Hydrological Processes, vol. 14, pp. 1357–1369, John Wiley & Sons Ltd., 2000.

Gat, J. R.: Isotope Hydrology - A study of the water cycle, edited by T. K. Wei, Published by Imperial College Press and
735   distributed by World Scientific Publishing Co., Singapore., 2010.

Gat, J. R., Bowser, C. J. and Kendall, C.: The contribution of evaporation from the Great Lakes to the continental atmosphere: estimate based on stable isotope data, Geophys. Res. Lett., 21(7), 557–560, doi:10.1029/94GL00069, 1994.

Gibson, J. J. and Edwards, T. W. D.: Regional water balance trends and evaporation-transpiration partitioning from a stable isotope survey of lakes in northern Canada, Global Biogeochem. Cycles, 16(2), 10-1-10–14,
740   doi:10.1029/2001gb001839, 2002.

Graf, P., Wernli, H., Pfahl, S. and Sodemann, H.: A new interpretative framework for below-cloud effects on stable water isotopes in vapour and rain, Atmos. Chem. Phys., 19(2), 747–765, doi:10.5194/acp-19-747-2019, 2019.

Griffis, T. J., Wood, J. D., Baker, J. M., Lee, X., Xiao, K., Chen, Z., Welp, L. R., Schultz, N. M., Gorski, G., Chen, M. and Nieber, J.: Investigating the source, transport, and isotope composition of water vapor in the planetary boundary layer,

745   Atmos. Chem. Phys., 16(8), 5139–5157, doi:10.5194/acp-16-5139-2016, 2016.

He, H. and Smith, R. B.: Stable isotope composition of water vapor in the atmospheric boundary layer above the forests of New England, J. Geophys. Res. Atmos., 104(D9), 11657–11673, doi:10.1029/1999JD900080, 1999.

Herrmann, H.: Kinetics of Aqueous Phase Reactions Relevant for Atmospheric Chemistry, Chem. Rev., 103(12), 4691–4716, doi:10.1021/cr020658q, 2003.

750   IAEA (2009): Reference Sheet for VSMOW2 and SLAP2 international measurement standards. Issued 2009-02-13, International Atomic Energy Agency, Vienna , 5 p., http://curem.iaea.org/catalogue/SI/pdf/VSMOW2_SLAP2 .pdf.

Jasechko, S., Sharp, Z. D., Gibson, J. J., Birks, S. J., Yi, Y. and Fawcett, P. J.: Terrestrial water fluxes dominated by transpiration, Nature, 496(7445), 347–350, doi:10.1038/nature11983, 2013.

Kendall, C. and Coplen, T. B.: Distribution of oxygen-18 and deuteriun in river waters across the United States, Hydrol.
755   Process., 15(7), 1363–1393, doi:10.1002/hyp.217, 2001.

Koscielny, A. J., Doviak, R. J. and Zrnic, D. S.: An Evaluation of the Accuracy of Some Radar Wind Profiling Techniques, J. Atmos. Ocean. Technol., 1(4), 309–320, doi:10.1175/1520-0426(1984)001<0309:AEOTAO>2.0.CO;2, 1984.

Kottmeier, C., Kalthoff, N., Barthlott, C., Corsmeier, U., Van Baelen, J., Behrendt, A., Behrendt, R., Blyth, A., Coulter, R., Crewell, S., Di Girolamo, P., Dorninger, M., Flamant, C., Foken, T., Hagen, M., Hauck, C., Höller, H., Konow, H.,
760   Kunz, M., Mahlke, H., Mobbs, S., Richard, E., Steinacker, R., Weckwerth, T., Wieser, A. and Wulfmeyer, V.: Mechanisms initiating deep convection over complex terrain during COPS, Meteorol. Zeitschrift, 17(6), 931–948, doi:10.1127/0941-2948/2008/0348, 2008.

Lesouëf, D., Gheusi, F., Chazette, P., Delmas, R. and Sanak, J.: Low Tropospheric Layers Over Reunion Island in Lidar-Derived Observations and a High-Resolution Model, Boundary-Layer Meteorol., 149(3), 425–453, doi:10.1007/s10546-
765   013-9851-9, 2013.

Majoube, M.: Fractionnement en oxygène 18 et en deutérium entre l'eau et sa vapeur, J. Chim. Phys., 68, 1423–1436, doi:10.1051/jcp/1971681423, 1971.

Mayr, G. J., Armi, L., Gohm, A., Zängl, G., Durran, D. R., Flamant, C., Gaberšek, S., Mobbs, S., Ross, A. and Weissmann, M.: Gap flows: Results from the Mesoscale Alpine Programme, Q. J. R. Meteorol. Soc., 133(625), 881–896,
770   doi:10.1002/qj.66, 2007.

Noone, D.: Pairing measurements of the water vapor isotope ratio with humidity to deduce atmospheric moistening and dehydration in the tropical midtroposphere, J. Clim., doi:10.1175/JCLI-D-11-00582.1, 2012.

Raut, J.-C. C. and Chazette, P.: Assessment of vertically-resolved PM10 from mobile lidar observations, Atmos. Chem. Phys., 9(21), 8617–8638, doi:10.5194/acp-9-8617-2009, 2009.

775   Salmon, O., Welp, L. R., Baldwin, M., Hajny, K., Stirm, B. and Shepson, P.: Vertical profile observations of water vapor deuterium excess in the lower troposphere, Atmos. Chem. Phys., 19(17), 11525–11543, doi:10.5194/acp-19-11525-2019, 2019.

Sodemann, H., Aemisegger, F., Pfahl, S., Bitter, M., Corsmeier, U., Feuerle, T., Graf, P., Hankers, R., Hsiao, G., Schulz, H., Wieser, A. and Wernli, H.: The stable isotopic composition of water vapour above Corsica during the HyMeX SOP1
780   campaign: Insight into vertical mixing processes from lower-tropospheric survey flights, Atmos. Chem. Phys., 17(9), 6125–6151, doi:10.5194/acp-17-6125-2017, 2017.

Steen-Larsen, H. C., Johnsen, S. J., Masson-Delmotte, V., Stenni, B., Risi, C., Sodemann, H., Balslev-Clausen, D., Blunier, T., Dahl-Jensen, D., Ellehøj, M. D., Falourd, S., Grindsted, A., Gkinis, V., Jouzel, J., Popp, T., Sheldon, S., Simonsen, S. B., Sjolte, J., Steffensen, J. P., Sperlich, P., Sveinbjörnsdottír, Á. E., Vinther, B. M. and White, J. W. C.: Continuous
785   monitoring of summer surface water vapor isotopic composition above the Greenland Ice Sheet, Atmos. Chem. Phys., 13(9), 4815–4828, doi:10.3929/ethz-b-000067919, 2013.

Steen-Larsen, H. C., Sveinbjörnsdottir, A. E., Peters, A. J., Masson-Delmotte, V., Guishard, M. P., Hsiao, G., Jouzel, J., Noone, D., Warren, J. K. and White, J. W. C.: Climatic controls on water vapor deuterium excess in the marine boundary layer of the North Atlantic based on 500 days of in situ, continuous measurements, Atmos. Chem. Phys., 14(15), 7741–7756,
790   doi:10.5194/acp-14-7741-2014, 2014.

Totems, J., Chazette, P. and Raut, J.: Accuracy of current Arctic springtime water vapour estimates, assessed by Raman lidar, Q. J. R. Meteorol. Soc., 145(720), 1234–1249, doi:10.1002/qj.3492, 2019.

Weng, Y., Touzeau, A. and Sodemann, H.: Correcting the impact of the isotope composition on the mixing ratio dependency of water vapour isotope measurements with cavity ring-down spectrometers, Atmos. Meas. Tech., 13(6), 3167–3190,

795   doi:10.5194/amt-13-3167-2020, 2020.

Worden, J., Noone, D., Bowman, K., Beer, R., Eldering, A., Fisher, B., Gunson, M., Goldman, A., Herman, R., Kulawik, S. S., Lampel, M., Osterman, G., Rinsland, C., Rodgers, C., Sander, S., Shephard, M., Webster, C. R. and Worden, H.: Importance of rain evaporation and continental convection in the tropical water cycle, Nature, doi:10.1038/nature05508, 2007.

800

805 Table A1. Data available during the period of the field experiment between June 11 and 23, 2020. The cross "X" indicates that the ULA or instrument was operated on a half-day basis. The malfunctions are denoted by "M". The number of flights is indicated per ULM for each half-day. For in situ samplings, the number of samples per half-day is indicated. During the first two flights of the ULA-IC, the iMet sonde was not operating (denoted by orange numbers). A sequence of ULA-IC flights experienced saturation in the inlet, that requires data filtering (denoted by blue numbers).

Instrument		11	12	13	14	15	16	17	18	19	20	21	22	23
Ground-based measurements														
Lidar WALI			X	X	X	X	X	X	X	X	X	X	X	M
Wind lidar WLS100					X	X	X	X	X	X	X	X	X	X
Precipitation sampling		1	3	1		1	1	1	10			2	2	
Airborne measurements														
ULA-A				M	X	X	X	X	X	X	X	X	X	X
	ALiAS			1	1	2	1 1	2 2	2 1	2 1	1 1		1 1	1
ULA-IC				X	X	X	X	X	X	X	X	X		
	CRDS			1 1	1	1	1	1	1 2	1 1	2 1	1		
	CASCC				M		M			1	1	1	1	
UAV				1	1		1		1	1	1		1	
Boat measurements in the lake														
Temperature sounding				1			1	2	2	2	1	1	1	
Isotope sampling	Microlayer			1			1		1	1	1	M	1	
	2 m deep			1			1		1	1	1	1	1	
Boat measurements in the atmosphere														
CRDS													X	

810

Appendix B: Ultra-light aircraft flights description

Table B1. Flights characteristics for the remote sensing payload (ULA-A).

Flight	Date & time (LT*) dd/mm HHMM-HHMM	Maximum flight altitude during slow spiral ascent (km a.m.s.l.)	Comment
F01	12/06 1845-1850	-	Aborted
F02	13/06 1000-1200	3.5	Profile
F03	13/06 1800-1930	3.8	Profile & transverse
F04	14/06 1630-1700	2.5	Profile
F05	14/06 1730-1830	4.1	Profile
F06	16/06 1030-1100	3.5	Profile
F07	16/06 1700-1800	3.5	Profile & lake axis
F08	17/06 0900-0940	3.4	Profile
F09	17/06 1030-1150	3.7	Profile & transverse
F10	17/06 1545-1700	3.7	Profile & transverse
F11	17/06 1745-1900	3.7	Profile & transverse
F12	18/06 0830-0945	3.7	Profile
F13	18/06 1100-1230	3.7	Profile & transverse
F14	18/06 1550-1715	4.1	Profile & transverse
F15	19/06 0845-1005	3.5	Profile & transverse
F16	19/06 1115-1250	4.5	Profile
F17	19/06 1535-1720	3.7	Profile & other valley
F18	20/06 1210-1335	4.3	Profile & lake axis
F19	20/06 1620-1725	4.0	Profile & lake axis
F20	21/06 1130-1240	3.5	Profile & lake axis
F21	22/06 1100-1200	4.1	Profile
F22	22/06 1600-1650	3.6	Profile
F23	23/06 1120-1330	4.2	Profile & other valleys

*Local Time (LT)

815

Table B2. Flights characteristics for the in situ payload (ULA-IC).

Flight	Date & time (LT*) dd/mm HHMM-HHMM	Maximum flight altitude during slow spiral ascent (km a.m.s.l.)	Comment
F01	12/06 19:23-19:50	1.0	Local survey No iMet data
F02	13/06 10:25-12:50	1.6	Lake survey No iMet data
F03	13/06 18:22-19:49	2.2	Lake survey
F04	14/06 16:53-18:49	2.8	Lake survey
F05	16/06 16:30-18:44	2.6	Lake survey
F06	17/06 10:13-11:20	3.1	Lake survey
F07	17/06 16:35-18:20	3.6	Profiles
F08	18/06 10:30-11:31	2.4	Profiles
F09	18/06 11:56-12:51	3.5	Lake survey
F10	18/06 16:41-18:10	3.8	Clouds

			Partial isotope inlet saturation
F11	19/06 10:34-11:45	2.9	Profiles No isotope data due to isotope inlet saturation
F12	19/06 15:39-16:58	3.1	Lake survey Partial isotope inlet saturation
F13	19/06 17:49-19:18	4.7	Clouds Partial isotope inlet saturation
F14	20/06 11:04-12:39	3.5	Profiles Partial isotope inlet saturation
F15	20/06 14:49-17:16	3.4	Lake survey

*Local Time (LT)

Appendix C: Water vapor stable isotopes interpretive framework

820   The isotope composition $\delta\,^2H$ and $\delta^{18}O$ are given by the relationships:

$$
\begin{cases}
\delta\,^2H = \left. R_{^2H} \middle/ R^S_{^2H} \right. - 1 \\[2mm]
\delta^{18}O = \left. R_{^{18}O} \middle/ R^S_{^{18}O} \right. - 1
\end{cases}
\tag{C1}
$$

Where R^S_X is the isotope ratio of Vienna Standard Mean Ocean Water (VSMOW) for the compound X and R_X the isotopic ratio given by

$$
\begin{cases}
R_{^2H} = \left. H\,^2HO \middle/ H_2O \right. \\[2mm]
R_{^{18}O} = \left. H_2\,^{18}O \middle/ H_2O \right.
\end{cases}
\tag{C2}
$$

The d-excess (d) is therefore defined as

$$
d = \delta\,^2H - 8 \cdot \delta^{18}O
\tag{C3}
$$

to measure the deviation from equilibrium fractionation, noting the global average value for precipitation $d = 10‰$ (Dansgaard,
825   1964).

Appendix D: Water isotope data processing

D.1 Processing of liquid samples for stable water isotope analysis

Liquid water samples were processed at FARLAB, University of Bergen, according to established laboratory routines. For isotopic analysis, liquid water samples were transferred to 1.5 ml glass vials with rubber/PTFE septa (part #548-0907, VWR, USA). An autosampler (A0325, Picarro Inc) injected ca. 2 µl per injection into a high precision vaporizer (A0211, Picarro Inc, USA) heated to 110°C. After blending with dry N_2 (< 5 ppm H_2O) the gas mixture was directed into the measurement cavity of a Cavity-Ring Down Spectrometer (L2140-i, Picarro Inc, Sunnyvale, USA) for about 7 min with a typical water concentration of 20 000 ppm. Three secondary laboratory standards were measured at the beginning and end of each batch for calibration purposes. Batches consisted typically of 20 samples, with laboratory drift standard DI, measured every 5 samples. For calibration according to International Atomic Energy Agency recommendations (IAEA, 2009), 16 injections of the laboratory standards EVAP ($\delta^2H = 4.75\pm0.11‰$, $\delta^{18}O = 5.03\pm0.02‰$) and GSM1, were used, and averaged over the beginning and end of each batch for calibration. Typical short-term reproducibility is 0.3‰ for δ^2H and 0.04‰ for $\delta^{18}O$. Long-term measurement accuracy is better than 0.66‰ for δ^2H, 0.15‰ for $\delta^{18}O$, and 0.83‰ for the d-excess, evaluated from the 1-sigma standard deviation of the analysis of an internal laboratory standard over one year.

D.2 Processing of stable isotope measurements in water vapor

Raw measurements of pressure and water vapor mixing ratio of the CRDS (Picarro L2130-i, Ser. No. HIDS2254) were corrected using calibration functions established at the FARLAB laboratory, University of Bergen, Norway. Raw measurements of the isotope parameters, expressed as δ-values relative to VSMOW2 (Vienna Standard Mean Ocean Water 2), were corrected for the mixing ratio-isotope composition dependency using time-constant correction functions obtained for this analyzer according to the method of Weng et al. (2020). For calibration, vapor isotope data were transferred onto the VSMOW2-SLAP2 scale by routine measurements of secondary laboratory standards using a Picarro Standard Delivery Module (SDM, Part No. A0101, Picarro Inc.) before and after the campaign. Hereby, secondary laboratory standards GSM1 ($\delta^2H = -262.95\pm0.30‰$, $\delta^{18}O = -33.07\pm0.05‰$), and DI ($\delta^2H = -50.38\pm0.37‰$, $\delta^{18}O = -7.78\pm0.07‰$) were measured repeatedly for 20 min in the period 1 June 2019 to 19 July 2019 (Figure C1). Calibrations of the CRDS analyser in the laboratory before and after the field deployment showed minor drift during the measurement period (GSM1 $\delta^{18}O$: 0.002 ‰/month, DI $\delta^{18}O$: -0.233 ‰/month, GSM1 δ^2H: 1.045 ‰/month, DI δ^2H: -0.853 ‰/month). From 2-sigma standard deviations of all valid SDM calibrations, the combined calibration uncertainty is estimated to be on the order of 0.2‰ for $\delta^{18}O$ and 2‰ for δ^2H. A small bubbler system was used in the field for testing instrument drift before and after flight operations in the field. These tests indicated an anomaly in the CRDS measurements 18-20 June, partially affecting two flights in the morning of 19 June, and the first flight on 20 June. The anomaly was due to a saturated inlet system from condensate forming on the

aircraft during a cloud sampling flight on 18 June. Flight periods affected by the saturated inlet were excluded from further analysis, as well as the entire flight 11 of ULA-IC, and are indicated with a corresponding quality flag in the data files (Table B2).
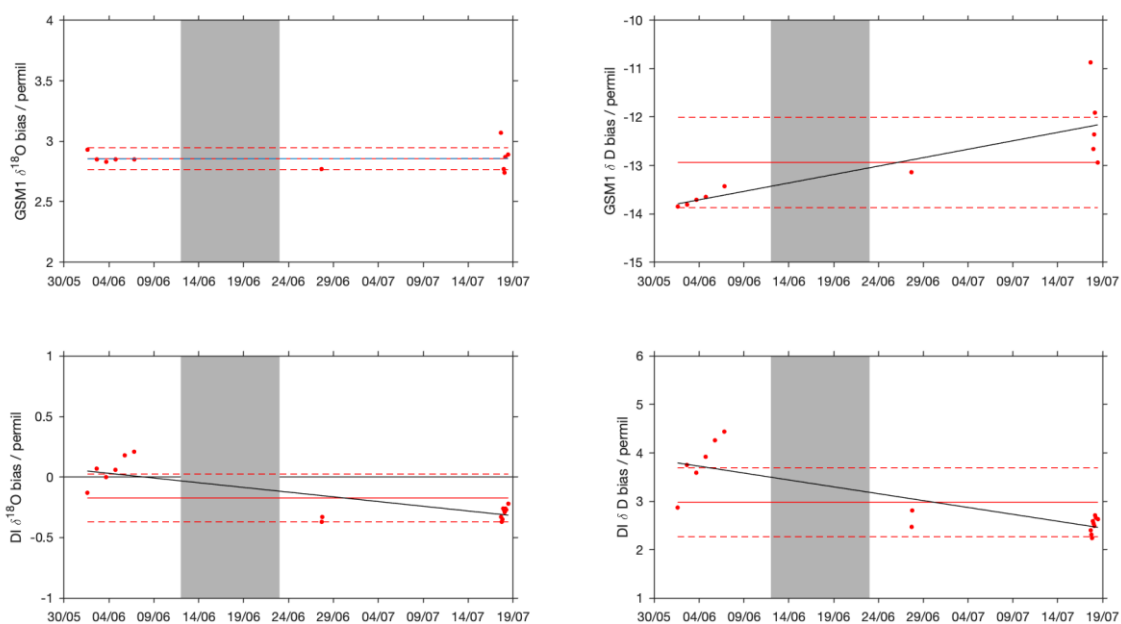
865 Figure C1: Bias between nominal and raw delta-values obtained with the Standards Delivery Module with working standards DI and GSM1 on analyzer HIDS2254 before and after the L-WAIVE campaign period. Grey area denotes campaign period. Red lines denote the mean and 1-sigma standard deviation of all valid SDM calibrations in the period 1 May 2019 to 19 July 2019. Black line is a linear regression line.

D.3 Sensitivity of CRDS instrument parameters to flight conditions
870

The CRDS analyser was mounted in the ULA frame without additional thermal insulation. Since the infrared spectrometry is sensitive to both, the pressure and temperature conditions in the measurement cavity, and the associated wavelength monitor (Gupta et al., 2009), we document here the potential impact of the exposed conditions on the ULA-IC measurement data at 2s time averaging. The cavity pressure in the CRDS is narrowly regulated to 50 Torr (66.67 hPa) on ground (Fig. C2a, black

875 area). During flight, the spread of the distribution widens due to turbulence and vertical motion of the aircraft, albeit without inducing a bias to the cavity pressure (grey shading). The cavity temperature is regulated to 80.00±0.02 °C on ground (Fig. C2b). During flight, a tail of lower temperatures develops, likely due to the constant cooling effect of airflow around the analyser, shifting the maximum of the distribution to slightly below 80°C (grey shading). Data points with cavity temperatures below 79.98°C can potentially be compromised, and have been flagged with a corresponding quality flag in the data set.

880 Temperature of the warm box, housing the wavelength monitor of the CRDS, is maintained to 45.00±0.02 °C on ground, with some deviations to warmer temperatures (Fig. C2c). During flight, the maximum of the distribution shifts to 0.01 K lower temperatures, while retaining an overall similar variability compared to ground condition (grey shading). The temperature within the analyser (Data acquisition system temperature, Fig. C2d) is not regulated, and therefore most strongly affected by ambient conditions. While the overall influence of in-flight conditions appears relatively limited, with the large majority of

885 data points remaining within specification range, insulation to the analyser housing could probably further increase stability of the instrument during flight. This will in particular be important for future operation of the ULA in colder climate zones, and other seasons.
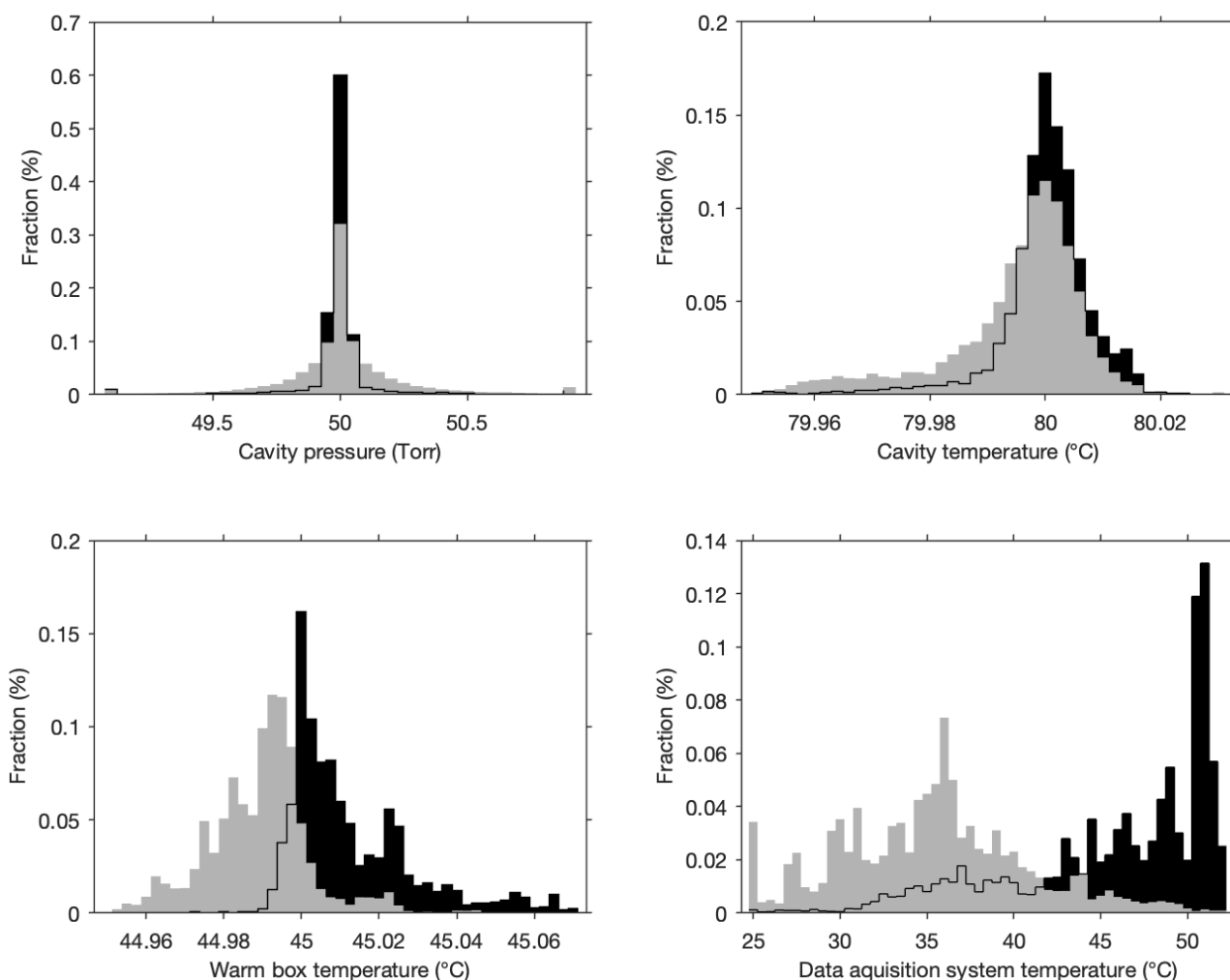
890 Figure D2: CRDS instrument parameters on ground and during flight with ULA-IC. (a) Distribution of cavity pressure (Torr), (b) cavity temperature (°C), (c) warm-box temperature (°C), and (d) data acquisition system temperature (°C) on ground (black)

and during flight segments with level or slowly changing altitude (sequence flag 1 or 2). Data are averaged to a 2 s time interval.

Appendix E: Lidar products description

The volume depolarisation ratio (VDR) is calculated following Chazette et al. (2012) for both lidars, WALI and ALiAS. It is retrieved with an absolute uncertainty of 0.2%. The VDR allows to highlight the particles that depolarize the radiation of the laser beam. These are particles that are not spherical, such as dust-like aerosols. The higher the VDR, the more the shape of the scatterers (molecules or aerosols) differs from a perfect sphere. The value of the molecular VDR corresponding to the WALI and ALiAS lidars is around 0.39% indicating that molecules cannot be considered as spherical scatters because their diffusion indicator is not perfectly isotropic. We use here the apparent scattering ratio ASR rather than the apparent backscatter coefficient because it is an indicator of scattering aerosol layers thanks to the molecular scattering correction. The ASR is given against the altitude z by the relationship:

$$ASR(z) = \left(1 + \frac{MBC(z)}{MBC(z) + ABC(z)}\right) \cdot e^{2 \cdot \overbrace{\int_{z_G}^{z} MSC(z')\cdot dz'}^{MOT(z)}} \tag{E1}$$

where MBC and MSC are the molecular backscatter coefficient and molecular scattering coefficients, respectively. MOT is the range-resolved molecular optical thickness and ABC is the aerosol backscatter coefficient.